Eindhoven University of Technology
Faculty of Technical Physics
Group Physics of Nanostructures

Characterisation of nonmagnetic and ferromagnetic tunnel junctions

N.C.W. Kuijpers

July 1998

Supervisor: Dr. ir. H.J.M. Swagten (EUT)
Professor: Prof. dr. ir. W.J.M. de Jonge (EUT)

Report of a graduation research project carried out in the group Physics of Nanostructures at the Eindhoven University of Technology (EUT), in collaboration with Philips Research Laboratories (PRL) in Eindhoven and the Francis Bitter Magnet Laboratory at the Massachusetts Institute of Technology in Cambridge, Massachusetts, U.S.A, during the period April 1997 until July 1998.

Contents

1 Introduction

1.1 General introduction

In 1988 a very large change in electrical resistance was observed when a magnetic field was applied to a multilayer consisting of a number of magnetic and nonmagnetic metallic layers. This effect is called Giant MagnetoResistance (GMR) and can be used for magnetic field detectors in recording media and for a non-volatile MRAM, as will be described in more detail in section 1.2.

Recently, a new large MR effect was discovered in *tunnel junctions*. This effect is called Tunnel MagnetoResistance (TMR) or Junction MagnetoResistance (JMR). Basically these junctions consist of three thin layers of which the bottom and the top layer are ferromagnetic and the sandwiched layer in between is a very thin insulator (e.g. Al_2O_3 with a thickness of about 10 Å to 30 Å), through which a quantum mechanical tunnelling current flows. The tunnelling current appears to depend on the relative alignment of the two ferromagnetic magnetisation vectors of the bottom and the top electrode.

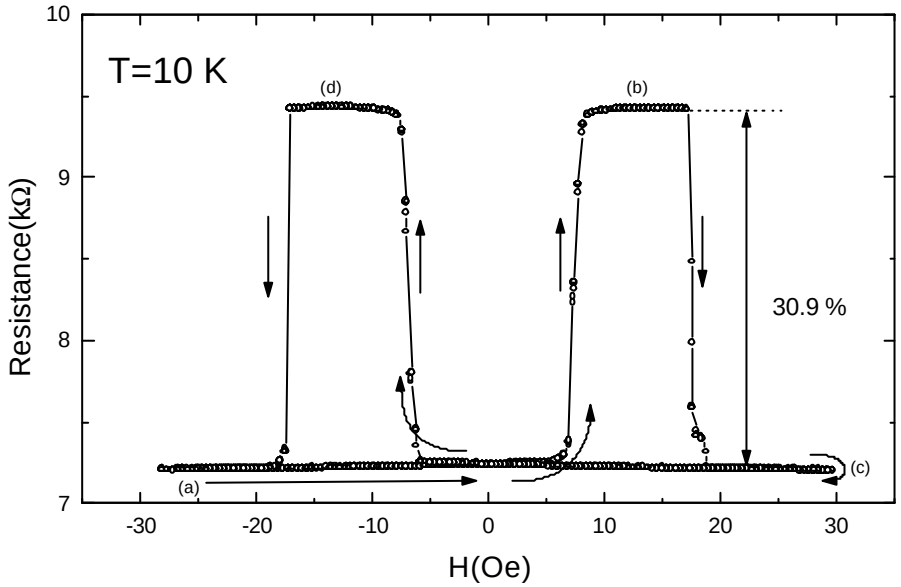

Figure 1.1 A typical MagnetoResistance measurement of a tunnel junction, performed at T=10 K. The MagnetoResistance is measured in the sequence a,b,c,d and back to a.

The actual pioneering experiments on magnetic tunnel junctions were performed by Julliere in the mid seventies. However, due to difficulties in fabrication of the ultrathin tunnelling barrier, the junctions did not exhibit a large and reproducible JMR effect. In 1995 Moodera from MIT managed to control the barrier preparation via a plasma oxidation of a thin Al layer. Figure 1.1 shows an example of a measurement of the resistance as a function of the magnetic field, measured at a temperature of 10 K on a tunnel junction prepared at MIT. It demonstrates that the resistance largely changes (in this example by 30.9 %) when a magnetic field is applied.

In this research project tunnel junctions prepared at MIT have been measured and analysed, which is the subject of the present graduation report. To begin with, chapter 2 and chapter 3 of this thesis will deal with the theoretical aspects of electrical tunnelling of a nonmagnetic tunnel junction and a magnetic tunnel junction, respectively. For nonmagnetic tunnel junctions a free electron model is assumed. For the magnetic tunnel junctions the model of Julliere, which described the JMR-effect phenomenologically, will be given. Also theoretical models of temperature dependence of the resistance and JMR will be presented in these chapters.

Chapter 4 describes the experimental methods used to prepare tunnel junctions and to perform measurements on them. The samples analysed in this report are prepared at the Francis Bitter Magnet Laboratory at the Massachusetts Institute of Technology in Cambridge, Massachusetts, U. S. A. The tunnel junctions are electrically sensitive and therefore the available equipment at the Eindhoven University had to be adjusted to measure tunnel junctions in a reliable and reproducible way.

Chapter 5 and chapter 6 present the electrical measurements on a nonmagnetic junction and on magnetic junctions, respectively. In these chapters we will show some basic characteristics of this type of junctions and how these compare with the models available in literature. The final section in chapter 6 will deal with the magnetic coupling of the ferromagnetic layers across the ultrathin insulating barrier, which is also determined via electrical measurements on tunnel junctions.

Chapter 7 deals with the electrical and magnetic properties of magnetic junctions as a function of the oxidation time of the aluminium interlayer. It is useful to know at what oxidation time the JMR is optimal. It will be shown that at a high oxidation time, beside the Al-oxide, also Co-oxide is formed which is able to impact both the resistance and the JMR significantly.

The last chapter of the report will give the main conclusions of this research project.

1.2 Technology assessment

The research in this project is focused on the physical properties of magnetic tunnel junctions. These junctions have two main fields of applications, (a) magnetic field detectors, and (b) Magnetic Random Access Memory (MRAM). Both applications are used for data storage and are described below.

Magnetic field detectors

Information technology is one of the fastest growing branches of the industry and pushes the storage of information to higher densities and faster access times. To reach those improvements the magnetic data storage structures become smaller, and as a consequence it is necessary to have more sensitive MagnetoResistive Heads (MRHs). In 1987 a new physical phenomenon called the Giant MagnetoResistive (GMR) effect was discovered. These structures show a large change in resistance when a magnetic field is applied. Recently (1997), IBM made the first commercial hard disk with a GMR head. One of the latest MagnetoResistive structures are the ferromagnetic tunnel junctions. Although tunnel MagnetoResistance (TMR) was discovered in the mid seventies by Julliere, it is only since a few years that preparation problems were solved, and reliable and reproducible JMR effects could be observed having a greater sensitivity and higher resistance than GMR.

Figure 1.2 shows a schematic representation of a tunnel magnetoresistive head in a data storage system. Writing is done with a conventional coil, and the domains are read out with a tunnelling read element.

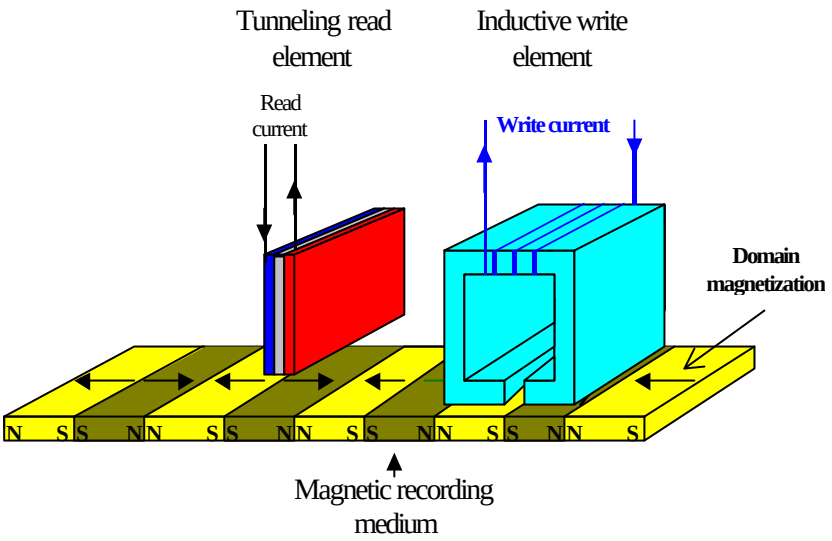

Figure 1.2 A magnetic recording system using Tunnel MagnetoResistance. Information is stored as different magnetisation directions of the domains on a recording medium. The domains are written with a conventional inductive write element and read out with a tunnelling read element.

Tunnel Magnetic Random Access Memory (tunnel-MRAM)

A MRAM architecture contains an array of memory cells, as schematic represented in figure 1.3. In a tunnel-MRAM the memory cells (as showed in the figure 1.3) are tunnel junctions which can be operated in two modes: the read operation or the write operation. When a cell is read, the output is either “0” or “1” which depends on the magnetic state of the cell. Because of their inherent simplicity of processing, non-volatility, static storage and non-destructive readout, MRAM can becomes advantageous above conventional DRAM in several applications. For more technical information about MRAM, see references [21-25].

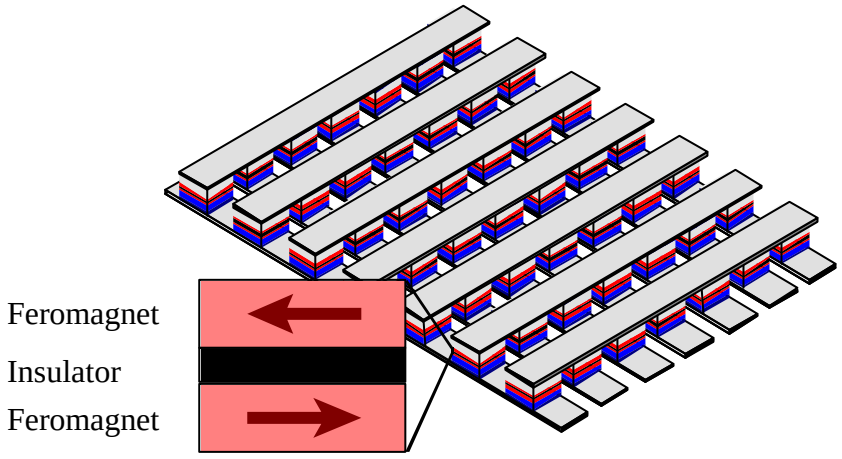

Figure 1.3 Schematic view of a magnetic random access memory (MRAM). One memory cell, (an individual tunnel junction) is zoomed out.

2 Nonmagnetic tunnelling theory

2.1 Introduction

This chapter describes the theory of the current density through nonmagnetic tunnel junctions. The theory of the current density and the magnetic properties of magnetic tunnel junctions will be described in the next chapter.

Section 2.2 of this chapter will deal with the fundamental aspects of tunnelling. First the definitions of the potential energy and bandstructure in metal-vacuum-metal junction will be given. The conductance of tunnel junctions takes place according to the laws of quantum mechanics; therefore a subsection will deal with the general quantum mechanics of tunnelling. In the next subsection a general formulation of the current density in a solid state will be derived, where a free electron approximation is assumed. The tunnelling probability will be modelled by the WKB-approximation. To close section 2.2, a qualitative approach of the electrical behaviour of tunnel junctions will be given.

The next section 2.3 will deal with quantitative expressions of the tunnel current. After some well-considered assumptions it is possible to derive analytical equations of the current-voltage (JV)-characteristics. These formulations are derived by Simmons [1] and Brinkman [4] and can be used for fitting on a JV-measurement to extract data of the junction tunnel barrier. The results of Simmons are the barrier width (in Ångstrom) and the barrier height (in eV). Brinkman gives the asymmetric barrier height as an extra barrier parameter. Also the deviations of the JV-characteristics due to a roughness of the interface are given. Finally a model of the RT-dependence of a tunnel junction, derived by Simmons, will be described.

2.2 The fundamental aspects of tunnelling

2.2.1 The potential energy and bandstructure in a metal-vacuum-metal junction

Figure 2.1 shows a schematic representation of the band structure of a metal-vacuum-metal junction. $V_{potential}$ is the potential energy of the electrons in the conductivity band. It can be seen that the potential barrier, j (x), of the insulator is higher than the Fermi energies, $E_{fermi\ L}$ and $E_{fermi\ R}$. The only way electrons can move from one electrode to the other is by means of tunnelling through the barrier.

x_L and x_R are the kinetic energies of the Fermi level of a electron in the metals on the left side and the right side, respectively. The Fermi energy is defined as the total energy of an electron in the Fermi level: $E_{fermi} = x + V_{potential}$. If there is no applied voltage the Fermi energies on both sides of the insulator are equal, and there is no net current.

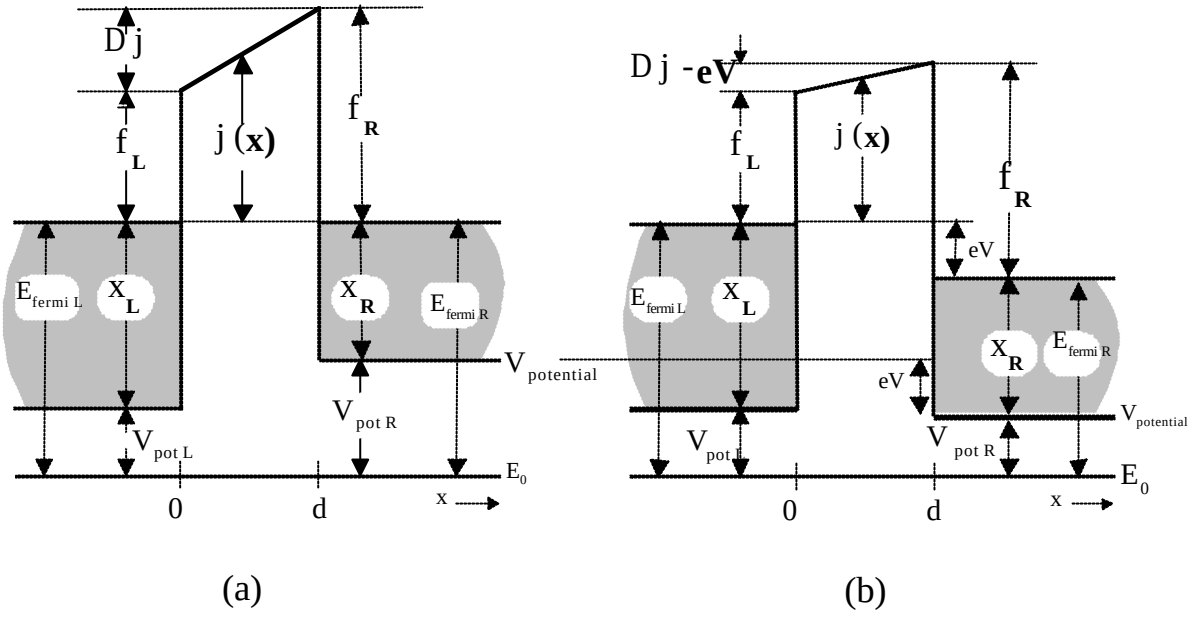

figure 2.1 Schematic representation of the one dimensional band structure of a metal-vacuum-metal junction, (a) without an applied voltage bias, (b) with an applied voltage bias (eV). More details about the variables are denoted in the text.

The difference between the Fermi energy level and the vacuum energy level is called the workfunction f, depends on the type of metal. The workfunctions are independent of the applied voltage. The barrier height j (x) is defined as the potential energy above the Fermi level on the left side of the insulator. If two different metals are used the difference in workfunctions on both sides of the insulator results in a trapezoid barrier, with an asymmetry in the barrier height of Dj .

By applying a voltage V (see figure 2.1) an energy difference of eV is created between the Fermi levels in the left and the right electrode. This give rise to a net tunnel current, which properties will be described in the following sections. By definition $E_{fermi\,L}$ remains constant and $E_{fermi\,R}$ changes. Also the $V_{potential}$ and the Dj change due to the applied voltage.

2.2.2 General quantum mechanic tunnelling

The three dimensional schrödinger equation of a one dimensional potential is given by

$$-\frac{\hbar^2}{2m}\nabla^2 y + V(x)y = E_{total}y \qquad (2.1)$$

where $\hbar$ = planck's constant ($\cong 1.0 \cdot 10^{-34}$ Js) ,
y = wave function,
$V(x)$= potential energy of the electron (V) (see figure 2.2),
E_{total}= total energy of the electron (J) (potential and kinetic energy).

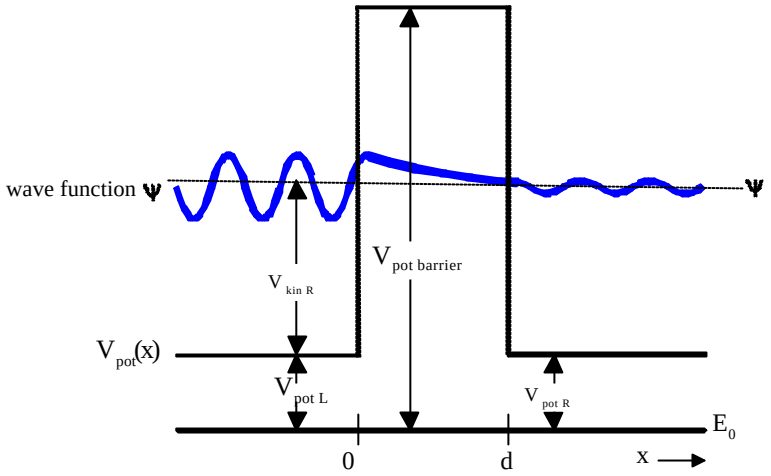

Figure 2.2 The wave function of a electron tunnelling through a barrier, where the electron moves from the left to the right.

The wave vector y can be written as $y = X(x)Y(y)Z(z)$ which gives the following equation:

$$-\frac{\hbar^2}{2m}\left[\frac{1}{X}\frac{\partial^2 X}{\partial x^2}+\frac{1}{Y}\frac{\partial^2 X}{\partial x^2}+\frac{1}{Z}\frac{\partial^2 Z}{\partial x^2}\right]+V(x)-E_{total}=0\,. \tag{2.2}$$

Separation of variables gives three one-dimensional problems:

$$-\frac{\hbar^2}{2m}\left[\frac{1}{X}\frac{\partial^2 X}{\partial x^2}\right]+V(x)+E_{kin,y}+E_{kin,z}-E_{total}=0 \tag{2.3}$$

$$-\frac{\hbar^2}{2m}\left[\frac{1}{Y}\frac{\partial^2 Y}{\partial y^2}\right]=E_{kin,y} \tag{2.4}$$

$$-\frac{\hbar^2}{2m}\left[\frac{1}{Z}\frac{\partial^2 Z}{\partial z^2}\right]=E_{kin,z} \tag{2.5}$$

After solving the equations the wave vectors become

$$k_x=\sqrt{\frac{2m}{\hbar^2}\left(E_{tot}+E_{kin,y}-E_{kin,z}-V(x)\right)};\; k_y=\sqrt{\frac{2m}{\hbar^2}\left(E_{kin,y}\right)};\; k_z=\sqrt{\frac{2m}{\hbar^2}\left(E_{kin,z}\right)}.$$

It can be seen that the wave vectors k_y and k_z (also noted as $k_{||}$ because these waves are directed parallel to the insulator) before and after tunnelling are conserved. The second conserved property is the total energy of the tunnelling electron.

2.2.3 Current density in a solid state

Figure 2.3 shows a schematically preview of an arriving electron moving from the left to the right. There are three wave functions: the wave functions of the arriving electron on the left side of the

barrier ($y_{L\rightarrow}$), the transmitted electron on the right side of the barrier ($y_{R\rightarrow}$), and the reflected electron on the left side of the barrier ($y_{L\leftarrow}$).

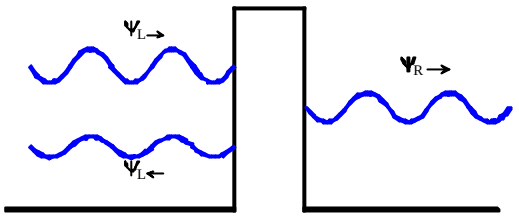

Figure 2.3 The wave functions of the arriving electron ($y_{L\rightarrow}$), the transmitted electron ($y_{R\rightarrow}$) and the reflected electron ($y_{L\leftarrow}$).

The transmission probability is defined as the probability that an arriving electron is transmitted. The transmission probability $|T|^2$ of an electron moving from the left to the right becomes:

$$\left|T(E_x)\right|^2 \equiv \frac{\left|y_{R\rightarrow}\right|^2}{\left|y_{L\rightarrow}\right|^2}. \tag{2.6}$$

A positive current direction is defined as a current from the right side to the left side of the barrier. The tunnelling current density of an electron in one state $\vec{k}$ with kinetic energy E is the charge that is transmitted through the barrier per seconds, and is equal to

$$e\left|T(E_x)\right|^2 \cdot v_x(E), \tag{2.7}$$

where $v_x(E)$ is the group velocity in the x-direction of the electron in state $\vec{k}$ which (quantum mechanically) is

$$v_x(E) = \frac{1}{\hbar}\left(\frac{\partial E}{\partial k_x}\right). \tag{2.8}$$

Because $E = E_x(k_x) + E_y(k_y) + E_z(k_z)$ this is equal to

$$v_x(E) = \frac{1}{\hbar}\left(\frac{\partial E_x}{\partial k_x}\right). \tag{2.9}$$

The current density of one state becomes

$$J = \frac{e}{\hbar}\left|T(E_x)\right|^2\left(\frac{\partial E_x}{\partial k_x}\right). \tag{2.10}$$

The total current density of a tunnel junction caused by electrons tunnelling from the left to the right can be calculated if the tunnelling current of all states in a band are summated. The summation over the wave numbers $\vec{k}$ must be multiplied by 2 because there are 2 spin states, spin up and spin down, at

one $\vec{k}$ state. In the band model the current of one state with energy E flowing from the left electrode the right electrode depend also on (1) the occupation of the states on the left side, defined by the Fermi-Dirac distribution $f_L(E)$ and (2) on the occupation of holes of the right electrode, defined by $(1-f_R(E))$. Now the total current density becomes

$$J_{LR} = 2e\sum_{\vec{k}} f_L(E)(1-f_R(E))\,|T(E_x)|^2\,\frac{1}{\hbar}\left(\frac{\partial E_x}{\partial k_x}\right). \tag{2.11}$$

For a free electron model the density of states $r(\vec{k}) = 1/(2p)^3$ is taken. The current density caused by tunnelling from the left to the right side of the barrier can now be written in an integral form as

$$J_{LR} = \frac{2e}{(2p)^3}\int\int\int d^3k\, f_L(E)(1-f_R(E))\frac{1}{\hbar}\left(\frac{\partial E_x}{\partial k_x}\right)|T(E_x)|^2\,, \tag{2.12}$$

which is equal to

$$J_{LR} = \frac{2e}{(2p)^3\hbar}\int\int\int d^2k_{\|}dE_x\, f_L(E)(1-f_R(E))\,|T(E_x)|^2\,. \tag{2.13}$$

In the same way the current density caused by tunnelling from the right to the left side can be written as

$$J_{RL} = -\frac{2e}{(2p)^3\hbar}\int\int\int d^2k_{\|}dE_x(1-f_L(E))\,f_R(E)\,|T(E_x)|^2\,. \tag{2.14}$$

The total current is the sum of both currents and becomes

$$J_{total} = J_{LR} + J_{RL} = \frac{2e}{(2p)^3\hbar}\int\int\int d^2k_{\|}dE_x(f_L(E)-f_R(E))\,|T(E_x)|^2\,. \tag{2.15}$$

The Fermi functions on the left side and on the right side are related by the following equation (see figure 2.1)

$$f_R(E) = f_L(E+eV) \equiv f(E+eV)\,. \tag{2.16}$$

The total current can thus be written as

$$J_{total} = \frac{2e}{(2p)^3\hbar}\int\int\int d^2k_{\|}dE_x(f(E)-f(E+eV))\,|T(E_x)|^2\,. \tag{2.17}$$

The current can be calculated in different ways, but eventually they all give the same result. As an example, we will show two other expressions of the current densities as calculated by Harrison [3] and Simmons [1]. First the expression of Harrison is

$$J_{harrison} = \frac{4pe}{\hbar} \sum_{k_{\|}} \int_{-\infty}^{+\infty} |T(E_x)|^2 \times [f(E) - f(E - eV)] dE_x \,. \tag{2.18}$$

It can directly be seen, using the two dimensional density of states $r(\vec{k}_{\|}) = 1/(2p)^2$, that this expression is the same as equation (2.17). It can be seen in appendix A that equation (2.17) is also the same expression of the current density as the one Simmons derived:

$$J_{simmons} = \frac{2em}{(2p)^2 \hbar^3} \int_{-\infty}^{-\infty} (f(E) - f(E - eV)) dE_r \int_{-\infty}^{-\infty} |T(E_x)| dE_x \,. \tag{2.19}$$

Binkman [4] and Simmons [1] use equation 2.18 and 2.19, respectively to derive an analytical expressions of the current density, which will be described in section 2.3.

2.2.4 Tunnelling probability by the WKB approximation

The WKB (Wentzel, Kramers, Brillouin) approximation assumes that the potential of the barrier, $j(x)$, varies rather slowly in comparison to variations in the wave function of a tunnelling electron. The general one-dimensional WKB transmission probability of a tunnelling electron is

$$|T(E_x)|^2 = \exp\left(-\frac{2}{\hbar} \int_0^d \{[h + j(x) - E_x] 2m\}^{1/2} dx \right), \tag{2.20}$$

where

E_x = The potential energy and kinetic energy of the electron perpendicular to the direction of the plane (see figure 2.1),

$j(x)$ = the potential energy of the barrier above the Fermi level,
m = the effective mass of the electron,
h = the total energy of the Fermi-level (see E_{fermiL} in figure 2.1),

d = the barrier width.

It can be seen that the transmission probability has an exponential dependence in the barrier width (d) and the square of the barrier height (j).

2.2.5 Qualitative JV characteristic

At zero Kelvin it can be seen from equation (2.18) that only electrons in the states between the Fermi energies of the left and the right side give rise to a net current. If the applied voltage is small ($|V| << j/e$), see figure 2.4a, the transmission probability of the energy states between the two Fermi states is practically constant. The number of states between the Fermi-energies of the left and the right side rises linear as a function of V, and due the constant tunnel probability of those states, this will give rise to a linear current density as a function of V as shown in figure 2.4c.

If the applied voltage gets larger, (but still $|V| < j/e$) see figure 2.4b, two effects happens:

(1) An applied voltage results in a lowering of the mean barrier height. This will give an exponential rising of the transmission probability of the Fermi-states as a function of the applied voltage.

(2) The transmission probability of the highest Fermi state is much higher than the transmission probability of the Fermi state of the electrode on the other side. This difference is a result of the exponential dependence in the barrier height of the tunnelling transmission (see equation 2.20). As a consequence the transmission electrons in the highest Fermi state carries the major current.

Due to (1) and (2) the current density will also rise exponentially as a function of the voltage. This give rise to an increasing and curved current density as the voltage gets larger (as shown in figure 2.4c).

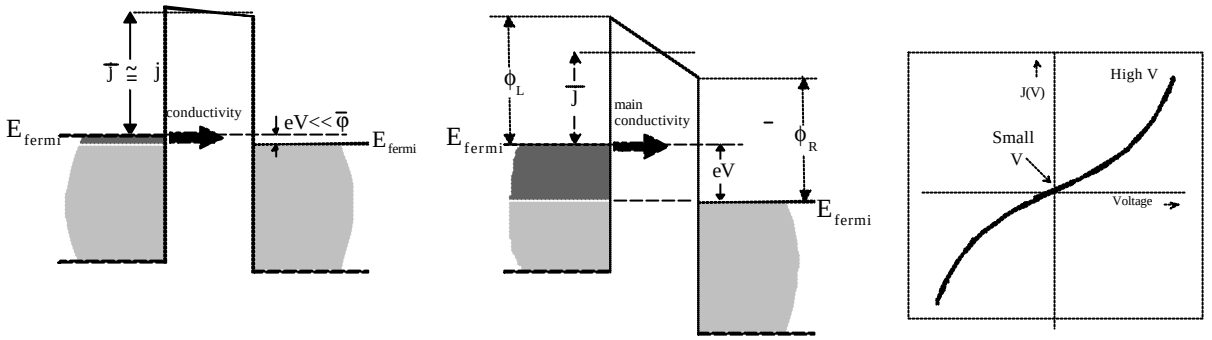

Figure 2.4 (a) Tunnelling in the voltage range $V << j/e$. (b) Tunnelling in the higher voltage range, but still $V < j/e$, the mean barrier height gets lower. (c) A qualitative JV-characteristic of a tunnel junction. The small voltage range $V << j$ results in a linear JV-characteristic. The higher voltage range results in a increasing and curved JV-characteristic.

The RT-characteristic of tunnel junctions caused by Fermi-Dirac statistics can also be explained qualitatively. In the intermediate voltage range ($V < j/e$) the main current density is caused by transmission of electrons in the highest Fermi level. If the temperature increases, more states will be occupied above the main Fermi level, with a higher tunnel probability, and this will raise the current density.

2.3 Analytical tunnel formula's

2.3.1 Simmons analytical JV-equation

Simmons [1] derived an analytical expression for the tunnel current density at zero Kelvin. To derive this expression, Simmons first derived equation (2.19) as a basis. This equation was applied to the problem of the WKB transmission probability of a rectangular barrier. He modelled a junction barrier as a rectangular barrier of which the height is equal to the mean $\bar{j}$ of the junction. This mean barrier height is defined as

$$\bar{j}(x) = \frac{1}{d}\int_0^d j(x)dx. \qquad (2.21)$$

where d is the barrier width and j (x) is the potential of the barrier, as denoted in figure 2.5.

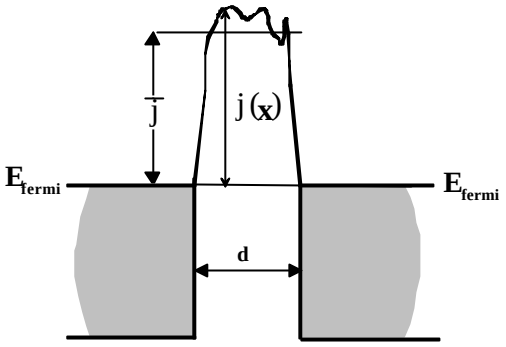

Figure 2.5 Definition of the mean barrier width, $\bar{J}$.

Using the WKB-equation (2.20), and making a Taylor series in the exponential term the transmission probability of a tunnelling electron becomes

$$\left|T(E_x)\right|^2 \approx \exp\left[-A\sqrt{h+\bar{J}-E_x}\right], \tag{2.22}$$

where

$A=\frac{2bd}{\hbar}\sqrt{2m}$ and β is a correction factor, which in first order is equal to

$$b = 1-\frac{1}{8(h+\bar{J}+E_x)^2 d}\int_0^d [j-\bar{J}]^2\,dx\,. \tag{2.23}$$

Simmons made a few assumptions:

(a) The energy of the Fermi state is much higher than eV, where V is the applied voltage.

(b) $A(j+eV)^{1/2}+1 \approx A(j+eV)^{1/2}$, or in other words $A(j+eV)^{1/2} >> 1$. The height and thickness of the junctions in this report are $d \approx 15$ Å and $j \approx 2$ eV, and thus

$$A(j+eV)^{1/2} \approx \frac{2\cdot 15\cdot 10^{-10}}{10^{-34}}\cdot\sqrt{2\cdot 9\cdot 10^{-31}}\cdot\sqrt{2\cdot 1.6\cdot 10^{-19}} = 23.$$

So this approximation is reasonable.

After some mathematics and taking the assumptions into account, the current density is analytically expressed by

$$J = J_0\left\{\bar{J}\exp(-A\bar{J})-(\bar{J}+eV)\exp\left[-A(\bar{J}-eV)^{1/2}\right]\right\}, \tag{2.24}$$

where $J_0 = e/(2p)^2\hbar(bd)^2$.

Assuming for j a rectangular potential barrier at V=0, with a constant barrier height, thus j (x)=j_0 at V=0. In an intermediate voltage range, where $|V|<j_0/e$, the mean barrier height is equal to $\bar{J} = (j_0 - eV/2)$, and equation (2.24) becomes

$$J = J_0 \left\{ \left(\bar{J} - \frac{eV}{2} \right) \exp\left[-A\left(\bar{J} - \frac{eV}{2} \right)^{1/2} \right] - \left(\bar{J} + \frac{eV}{2} \right) \exp\left[-A\left(\bar{J} + \frac{eV}{2} \right)^{1/2} \right] \right\}. \qquad (2.25)$$

The correction factor b can be calculated and is given by

$$b = 1 - (eV)^2 / 96(j_0 + h - E_x - eV/2)^2. \qquad (2.26)$$

If β is set to unity, the error made in b is 6% with $V = j_0/e$ and $E_x = h$ (the Energy of the electron E_x is equal to the energy of the Fermi level h) The error in b reduces rapidly if V gets lower, and is 1% with $V = 0.75\ j_0/e$, so it is a reasonable approximation to take $b = 1$. With $b = 1$, now equation (2.25) is expressed in practical units, usable for numerical calculations, and becomes

$$\Im(V) = 6.32 \cdot 10^{10} \frac{1}{s^2} \left\{ \left(p - \frac{V}{2} \right) \exp\left[-1.025\left(p - \frac{V}{2} \right)^{1/2} s \right] - \left(p + \frac{V}{2} \right) \exp\left[-1.025\left(p + \frac{V}{2} \right)^{1/2} s \right] \right\}, \qquad (2.27)$$

where

$\Im$ = current density expressed in A/cm^2,
s = insulator thickness in Ångstrom,
p = insulator mean height above the Fermi level in V.
V = applied voltage (V)
$6.32 \cdot 10^{10}$=constante (A/V)
1.025=constante ($m^{-1} V^{0.5}$)

In this project, this equation is used for numerical fitting of the JV-measurements and gives the barrier width and barrier height as fit parameters. Figure 2.6 shows an example of a JV-characteristic calculated by equation (2.27). It can be seen that the JV-characteristic gets curved as qualitatively predicted in section 2.2.5.

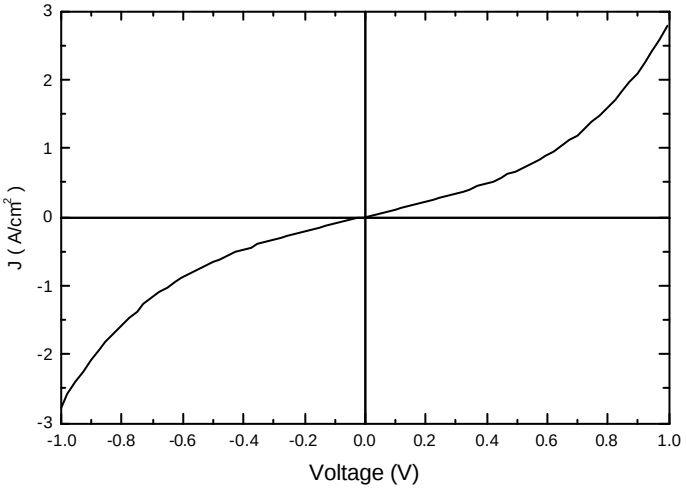

Figure 2.6 A typical JV-characteristic , calculated by Simmons equation (2.27). The barrier width s is 15 Å and the barrier height p is equal to 2 eV.

A Taylor expansion of equation (2.27) is derived to compare with the Taylor expression of Brinkman given in section 2.3.3. This expansion is given by (derived in appendix C)

$$\Im \approx 3.24 \cdot 10^{10} \frac{\sqrt{p}}{s} \cdot \exp(-1.025 \cdot s \cdot \sqrt{p})(V + 0.01094 \frac{s^2}{p} V^3), \qquad (2.28)$$

where the units of the variables are the same as in equation (2.27). It follows that the resistivity (R) at a small voltage becomes

$$R \approx \frac{1}{3.24 \cdot 10^{10}} \frac{s}{\sqrt{p}} \cdot \exp(1.025 \cdot s \cdot \sqrt{p}), \qquad (2.29)$$

where the units of the resistivity R is in Ω/cm^2. The resistivity as a function of the barrier width and height, calculated by this equation is plotted in figure 2.7.

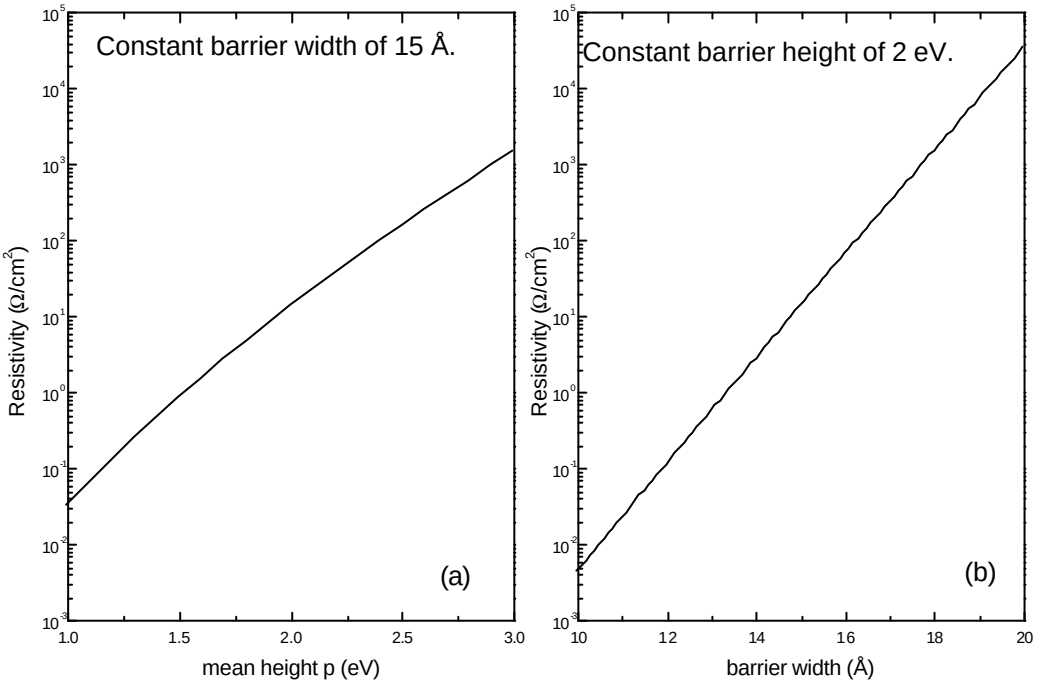

Figure 2.7 Resistivity of tunnel junctions as a function of the barrier width and height, calculated by equation (2.29). (a) Resistivity as a function of the mean height, with a constant barrier width of 15 Å. (b) Resistivity as a function of the barrier width, with a constant barrier height of 2 eV.

2.3.2 Current-Voltage characteristic of junction with a rough insulator surface

The tunnelling surface is in general not smooth but contains a certain roughness width. As a result of the exponential dependence of the transmission probability in the barrier width s (see equation 2.20), even a small variation in the barrier width creates a vast change of the transmission probability. Therefore there is also a vast different between the JV-characteristics of a junction with a rough surface insulator and a junction with a smooth surface (see figure 2.8). The JV-characteristic of a

junction with a rough interface is calculated. The Simmons equation in practical units (2.27) is used as a basis. If one assumes a Gaussian distribution of the insulator thickness with a variance of s (the roughness) and mean thickness s, the total current density becomes

$$\Im_s = \int_{-\infty}^{\infty} \Im(s+x) f_s(x) dx, \tag{2.30}$$

where $f_s(x)$ is the Gausian distribution of the film thickness, defined by

$$f_s(x) = \frac{1}{d\sqrt{2p}} e^{-\frac{x^2}{2s^2}}. \tag{2.31}$$

The $J_\sigma V$-characteristic of equation (2.30) can be written as

$$\begin{aligned}\Im_s = \frac{6.32\cdot 10^{10}}{s^2}\Big\{&(P-V/2)\exp\Big(-1.025\cdot(p-V/2)^{1/2}(s-0.5\cdot 1.025\cdot(p-V/2)^{1/2}s^2)\Big)\\ &-(P+V/2)\exp\Big(-1.025\cdot(p+V/2)^{1/2}(s-0.5\cdot 1.025\cdot(p+V/2)^{1/2}s^2)\Big)\Big\}\end{aligned} \tag{2.32}$$

It can directly be seen from equation (2.32) that taken s=0 gives the Simmons equation of (2.27), as expected. As the roughness (s) gets higher the current density ($\Im$) becomes higher. Figure 2.8 shows the effect of a roughness on the JV-equation calculated with formula (2.32).

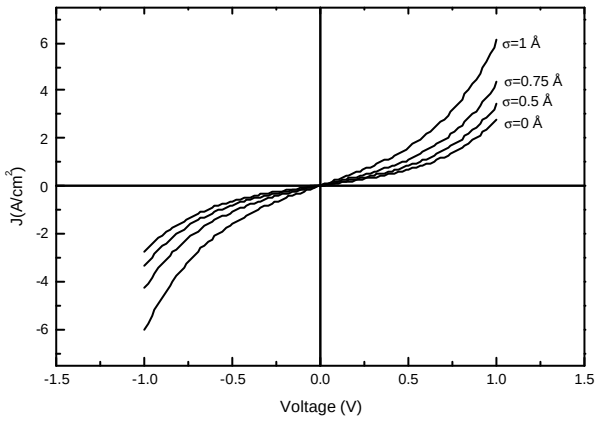

Figure 2.8 Effect of a roughness on the JV-curves, calculated by equation (2.32). All plots are JV-characteristics of junctions with a barrier height of 2 eV and mean width of 15 Å, only the roughness of the insulator is varied.

To abstract physical properties of a JV-measurement, the equation of Simmons (2.27) can be used and give the fit parameters s' and p'. However this equation takes no roughness into account, and as a consequence the fit parameters will deviate from the physical height (p) and mean width ($\bar{s}$) of the insulator. These deviations are defined by

$$\Delta s = s' - \bar{s} \text{ and } \Delta p = p' - p. \tag{2.33}$$

The deviations are derived in appendix B, and the final results are given by

$$\Delta s \approx -\frac{3}{4} c\sqrt{p}\, s^{2}, \tag{2.34}$$

and

$$\Delta p \approx -\frac{1}{2\bar{s}} c p^{1.5} s^{2}, \tag{2.35}$$

where c=1.02463. It can be seen that both *Ds* and *Dp* have a square dependence in σ.

Take for example a tunnel junction with a roughness of one monolayer, and therefore $s \approx 1$ Å, a barrier height of 2 eV and a mean barrier width of 15 Å (which are physical parameters). The errors in the extracted barrier parameters found by a numerical fit of the equation of Simmons to the measured JV-curve can be calculated by equations (2.35) and (2.34) and yields *Ds*=-1.1 Å and *Dp*=-0.1 eV. Thus the extracted parameters are a barrier width of 13.9 Å and a barrier height of 1.9 eV, calculated with equation (2.33) and deviate by less than 10 % from the actual parameters due to a small roughness.

2.3.3 Brinkmans analytical JV-equation

Brinkman [4] gives, analogous to Simmons, an analytical expression of the JV-characteristics of a junction. To take a bimetallic interface into account, he worked with an asymmetric trapezoid barrier with an asymmetry defined by

$$\Delta j = j_R - j_L,$$

which can also be seen in figure 2.1 The barrier potential $j(x)$ becomes

$$j(x) = j_L + \frac{\Delta j\, x}{d}.$$

As a basis Brinkman uses the formula of Harrison (2.18). This expression was expanded in power of voltage. The original analytical formula of Brinkman is an expression of the differential conductivity (dJ/dV), and is given by

$$\frac{G(V)}{G(0)} = 1 - \left(\frac{A\Delta j}{16\bar{j}^{3/2}}\right) eV + \left(\frac{9}{128}\frac{A^2}{\bar{j}}\right)(eV)^2, \tag{2.36}$$

where

$$A = 4(2m)^{1/2} d / 3\hbar$$

and

$$G(0) = (7.9 \cdot 10^{9} \bar{j} / d) \exp(-2\sqrt{\frac{2m}{\hbar^2}} \cdot d\bar{j}^{1/2}).$$

It can be seen that if the barrier height is symmetric (*Dp*=0) the conductivity is a square function. After integration over *V*, the total *J(V)* becomes

$$J(V) = G(0)\left[V - \left(\frac{A\Delta j}{32\bar{j}^{3/2}}\right)(eV)^2 + \left(\frac{3}{128}\frac{A^2}{\bar{j}}\right)(eV)^3\right]. \qquad (2.37)$$

Where the mean barrier height $\bar{j}$ is defined as: $\bar{j} = \frac{j_L + j_R}{2}$. Equation (2.37) is expressed in practical units, for the sake of numerical calculations and becomes

$$\Im(V) = \tilde{G}(0)\left[V - \left(\frac{1}{2}\cdot Const_2\frac{s\Delta p}{\bar{p}^{3/2}}\right)V^2 + \left(\frac{1}{3}\cdot Const_3\frac{s^2}{\bar{p}}\right)V^3\right], \qquad (2.38)$$

where

$\Im$ = current density [A/cm^2],
V= applied voltage [V],
s= barrier thickness [Å],

$\bar{p}$ = mean barrier height defined as $\bar{p} = \frac{p_L + p_R}{2}$ [V]

Dp= barrier asymmetry [V],

$\tilde{G}(0) = (Const_1 \cdot \bar{p}^{1/2} / d)\exp(-Const_0 \cdot d\bar{p}^{1/2})$ [A/(V.cm^2)]

and the constants are

$Const_0 = 2\sqrt{\frac{2m}{\hbar^2}} \approx 1.02463$ [m^{-1}V$^{-0.5}$], $Const_1 = 3.15877\cdot 10^{10}$ [m^{-1}V$^{-1.5}$],

$Const_2 = 0.0426929$ [m^{-1}V$^{-1.5}$], $Const_3 = 0.0328083$ [m^{-2}V^{-2}].

The equation above is used for numerical fitting of JV-measurements, and gives the barrier width (s), mean barrier height ($\bar{p}$) (which is denoted as p in the following text of this report) and asymmetric height (Dp) of the barrier as results.

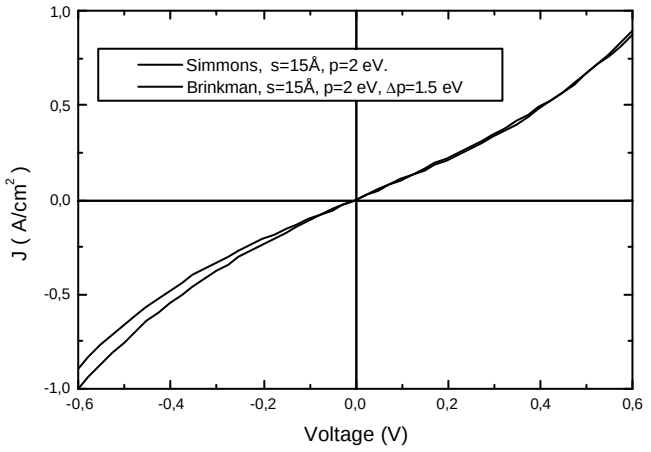

Figure 2.9 An example of a JV-curve of calculated by Simmons (2.27), and a JV-curve calculated by the equation of Brinkman (2.38). The JV-curve of Simmons does not take the asymmetric barrier into account.

For a symmetric barrier (Dp=0) the formula of Brinkman is approximately the same as the Taylor expression of the formula of Simmons (2.28) which applies for small voltages. But for asymmetric barriers the JV-characteristics of Simmons and Brinkman differ. This can be seen in figure 2.9 were a JV-curve of Simmons (equation 2.27) is compared with a curve of Brinkman (equation 2.38) with an

asymmetry of *Dp*=1.5 eV, yielding in the latter case in an asymmetric JV-characteristic. Note that the barrier width (*s*=15 Å) and the mean barrier height (*p*=2 eV) are for both curves are the same.

Appendix D gives an algorithm which reduce the computation time of the numerical fitting with the equation of Brinkman (2.38).

2.3.4 Simmons JT-equation

Simmons [2] derived a model for the thermal JT-tunnel characteristic with a small applied bias voltage. In his model he assumed the Fermi-Dirac statistics and a free electron model. He uses the WKB-probability of equation (2.20). This tunnel probability can also be written as

$$|T(E_x)|^2 = \exp\{-A\bar{j}^{1/2}[1+(h-E_x)/\bar{j}]^{1/2}\}. \tag{2.39}$$

Because the applied voltage is small ($eV << j$), only the electrons in the levels E_x close to h contribute effectively to the tunnel current. Therefore the factor $-A\bar{j}^{1/2}[1+(h-E_x)/\bar{j}]^{1/2}$ can be expanded in the first power of E_x and the tunnel probability can be written in an approximate form as:

$$|T(E_x)|^2 = \exp(-A\bar{j}^{1/2})\exp[-A(h-E_x)/2\bar{j}^{1/2}]. \tag{2.40}$$

As the basic for the calculation of the tunnel current Simmons uses equation (2.19). Taking the Fermi-Dirac distribution

$$f(E) = \frac{1}{\exp[(E-h)/kT]+1}, \tag{2.41}$$

the tunnel current becomes

$$J(V,T) = \frac{4\pi mekT}{h^3}\exp(-A\bar{j}^{1/2})\times \int_0^{E_m}\ln\left\{\frac{1+\exp[(h-E_x)/kT]}{1+\exp[(h-E_x-eV)/kT]}\right\}\times\exp\left[\left(-\frac{A}{2\bar{j}^{1/2}}\right)(h-E_x)\right]dE_x. \tag{2.42}$$

After some calculations and taking again the approximation $eV << j$ into account, Simmons derived the temperature dependence

$$J(V,T)/J(V,0) = \pi Ck T/\sin(\pi Ck T), \tag{2.43}$$

which can also be written as

$$R(J,T)/R(J,0) = \sin(\pi Ck T)/\pi Ck T, \tag{2.44}$$

where $B = \frac{4\pi^2 b\, s(2m)^{\frac{1}{2}}}{\hbar\bar{j}^{1/2}}$, k = constant of Boltzmann and $J(V,0)$ is the same current density as equation (2.25).

In practical units, taking b=1, equation (2.43) becomes

$$\Im(V,T)/\Im(V,0) = R(J,0)/R(J,T) = \frac{const \cdot s \cdot T}{p^{1/2}\sin\left(const \cdot \frac{s \cdot T}{p^{1/2}}\right)}, \qquad (2.45)$$

where $\Im(V,T)$ =current density (A/cm^2)

$const$=0.1386923117·10^{-3}

s=barrier width (Å)

p=barrier height (eV)

T=Temperature (K)

Figure 2.10 shows the temperature dependence of J and R calculate by equation (2.45).

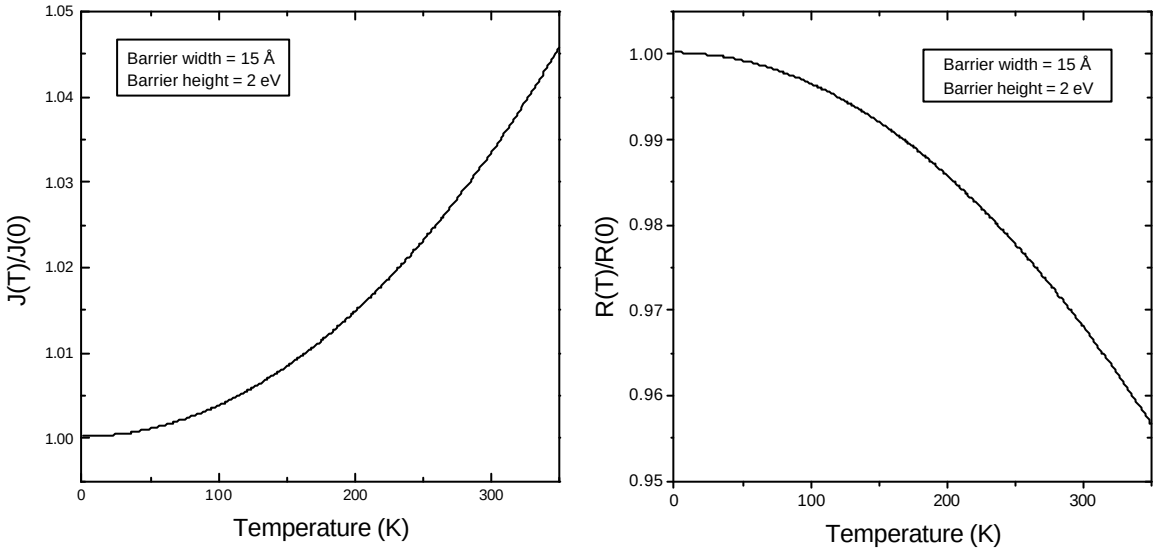

Figure 2.10 Temperature dependence of J and R, calculated by the model of Simmons, equation (2.45).

3 Magnetic spin polarised tunnelling theory

3.1 Introduction and model of Julliere

The tunnelling conductivity of electrons between two ferromagnetic electrodes, separated by a thin insulator, is dependent of the spin of the electrons. There are two spin directions of the electrons, namely spins up and spin down, and in ferromagnetic metals these electron spins occupy separated 3d bands as showed in figure 3.1. The splitting of the 3d bands is caused by the exchange coupling between the spin-up and spin-down electrons.

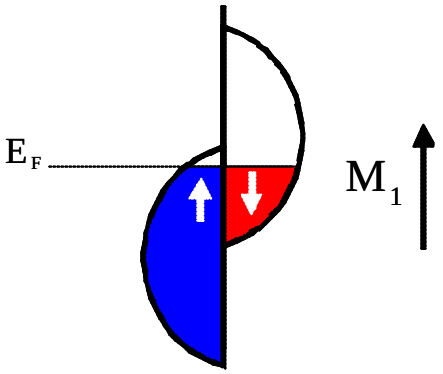

Figure 3.1 Splitting of 3d bands of a ferromagnetic electrode.

Ferromagnetic tunnel junctions have two electrodes. The magnetisation M of the electrodes can be parallel or antiparallel aligned. The electron bands of the parallel alignments are shown in figure 3.2a, and the antiparallel alignment are shown in figure 3.2b, where the tunnel barrier between the bottom electrode and the top electrode is schematically denoted as a dotted line.

The tunnelling current can be seen as a summation of a spin up and a spin down current. Tunnelling takes place only between bands with equal spins, as denoted by the curved arrows in figure 3.2. If there is no spin flip scattering, the current of one spin direction is conservative through whole the junction. In the pioneering experiments of Julliere [7] it was assumed that the tunnelling current of each spin direction is proportional to the product of the effective *tunnelling density of states* on both sides of the insulator. Note that this *tunnelling density of states* is an effective phenomenological parameter which must not be confused with the actual electron density of states at the Fermi energy level. Taking the assumption of Julliere into account, the tunnelling conductance (defined as $G=1/R$) of a parallel or antiparallel alignment becomes

$$G_p \propto N^+N^+ + N^-N^- \tag{3.1}$$

and

$$G_a \propto 2N^-N^+, \tag{3.2}$$

respectively, where $N+$ and $N-$ are the major and minor *tunnelling density of states*, respectively.

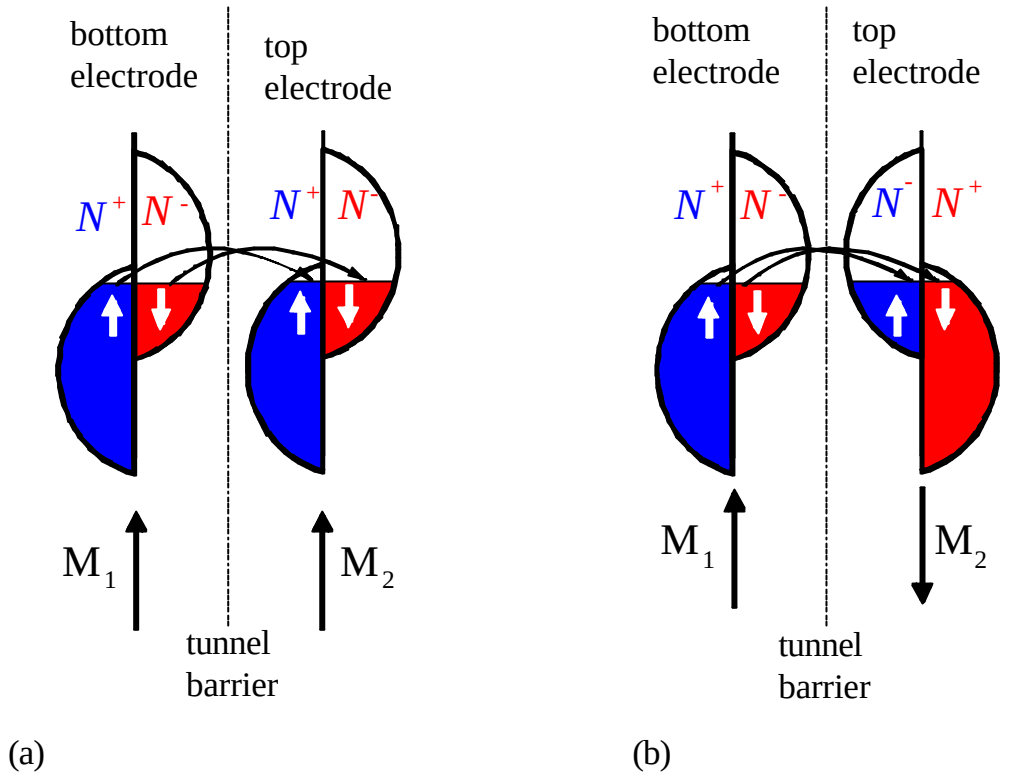

Figure 3.2 Band structure of the bottom and top electrodes. The dotted lines are a schematic notation of the tunnel barrier. N^+ and N^- are the 3d bands with the major and minor density of states, respectively. Two configurations of the electrodes are possible: (a) The electrodes are in the parallel alignment. (b) The electrodes are in the antiparallel alignment.

Equation 3.1 and 3.2 can also written as

$$G(q) \propto 1 + P_{top}P_{bottom}\cos(q)\,, \tag{3.3}$$

in which the equation is generalised for different polarisations of the top and bottom electrodes. q is the angle between the magnetisation directions of the two electrodes (q=0° or 180° for parallel or antiparallel magnetisations, respectively). P_{top} and P_{bottom} are the polarisations of the top and bottom electrodes, respectively, and defined as

$$P = \frac{N^+ - N^-}{N^+ + N^-} \tag{3.4}$$

The change in resistance or conductivity between the parallel and antiparallel alignment of the magnetic moments is *DR* or *DG*, respectively. This effect is expressed in the Junction MagnetoResistance (JMR), defined as

$$JMR \equiv \frac{\Delta R}{R_p} = \frac{\Delta G}{G_a}\,, \tag{3.5}$$

where R_p is the resistance in parallel alignment of the magnetisations of the electrodes and G_a is in the antiparallel alignment. The definition of the JMR by equation (3.5) is used throughout this report and

is expressed in percentages. With the Julliere model the JMR can be calculated by inserting equation (3.1) and (3.2) in equation (3.5) and yields

$$JMR = \frac{2P_{top}P_{bottom}}{1 - P_{top}P_{bottom}}, \tag{3.6}$$

At zero Kelvin the polarisation has been determined experimentally, yielding P_0=34±2% for Co and P_0=42±3% for $Ni_{80}Fe_{20}$ [11]. For these polarisations the theoretical JMR becomes 33% for a Co/insulator/NiFe junction, which compares favourably well with the existing experimental data [17] and the data in this report (see figure 6.8 and figure 7.4).

3.2 Temperature dependence of DG and G as a function of T

In the theory of Julliere the JMR does not depend on temperature, because in this model the polarisation of *P* of the magnetic electrodes is assumed to be temperature independent (see equation 3.6). This is not in accordance with existing data [11], that show a significant temperature difference between 5 K and 300 K, which is also concluded from the results of this report. Furthermore the temperature dependence of the conductivity due to broadening of the Fermi-distribution (as given in equation 2.43) is much weaker than seen in the experimental data for both nonmagnetic and magnetic tunnel junctions.

For these reasons Chang He Shang et al. [11] introduced a new model for the temperature dependence of the JMR and the conductivity, which will be described briefly in this section. The same equation of the conductivity as equation (3.3) is taken, but with an additional spin independent conductivity G_{SI}, which is not dependent of the magnetic alignment of the electrodes:

$$G(q) = G_T(1 + P_{top}P_{bottom}\cos(q)) + G_{SI}, \tag{3.7}$$

where G_T is the conductivity for direct elastic tunnelling, with a temperature dependence as derived in chapter 2, equation (2.43).

Unlike the model of Julliere, a temperature dependence of *P* is introduced which is proportional to the magnetisation of the electrode. In general it is stated that in approximation $M \propto (1 - aT^{3/2})$ if *T* is smaller than 0.4 T_c, arising from spin waves on the surface of the ferromagnetic electrode. Thus for the polarisation one may then write

$$P(T) = P_0(1 - aT^{3/2}). \tag{3.8}$$

The temperature dependence of *DG (=G(0°)–G(180°))* is easily derived from equation (3.7), and reads

$$\Delta G = 2G_T P_{top}P_{bottom}. \tag{3.9}$$

This quality does not contain G_{SI} and can be used straightforward to extract the polarisation and α of the bottom and the top electrodes from measurements of the resistance as function of the temperature.

Chang et al. found for the ferromagnetic films a_{Co}=1~6×10^{-6} K $^{-3/2}$ and a_{NiFe}=3~5×10^{-5} K $^{-3/2}$. For bulk the a of the same materials are comparable: a_{Co}=6.1×10^{-6} K $^{-3/2}$ and a_{NiFe}=1.23×10^{-5}K $^{-3/2}$ [11].

Further, the temperature dependence of G_{SI} can be calculated by

$$G_{SI} = < G > - G_T . \qquad (3.10)$$

In this formula $<G>$ is defined as the mean conductivity $< G >= (G_p(T) + G_a(T))/2$, where G_p and G_a are the conductivities in the parallel and antiparallel magnetisation alignments of the electrodes, respectively.

The theoretical understanding of the temperature dependence of the spin-independent contribution G_{SI} is far from complete. It is suggested in reference [11] that hopping due to imperfections in the Al_2O_3 barrier, may be an important mechanism. Due to hopping through a chain of N localised states, G_{SI} is proportional to a power law of the temperature: $G_{SI}(T) \mu T^{g}$, where g is given by $g(N)=N-(2/(N+1))$. Thus for N=2 we have g =4/3 and for N=3 we have g =5/2. In chapter 5 and 6 we will try to analyse the measured temperature dependence of the resistance, and we will see that G_{SI} is indeed proportional to a power law.

4 Experimental method

In the first section of this chapter the preparation of tunnel junctions will be described. Then a great deal of attention is paid to the central experimental technique used for our investigation, namely the MR (Magnetic Resistance) equipment. Finally a few words will be spent on MOKE (Magnetic Optical Kerr Effect).

4.1 Preparation of tunnel junctions

The tunnel junctions measured in this report were prepared at the Francis Bitter Magnet Laboratory at the Massachusetts Institute of Technology in Cambridge, Massachusetts, U.S.A, by J. S. Moodera and R. J. M. van de Veerdonk. First a general description of the preparation will be given.

The tunnel junctions were deposited by thermal evaporation in a high vacuum system with a base pressure of $2 \cdot 10^{-7}$ mTorr onto glass substrates, which can be cooled to near liquid nitrogen temperatures with a "cold finger" that is directly attached to the glass substrate. The thickness of the deposited layer was monitored by a quartz crystal monitor. Before the preparation, the glass substrate was cleaned in an oxygen glow discharge with a pressure of 70 mTorr.

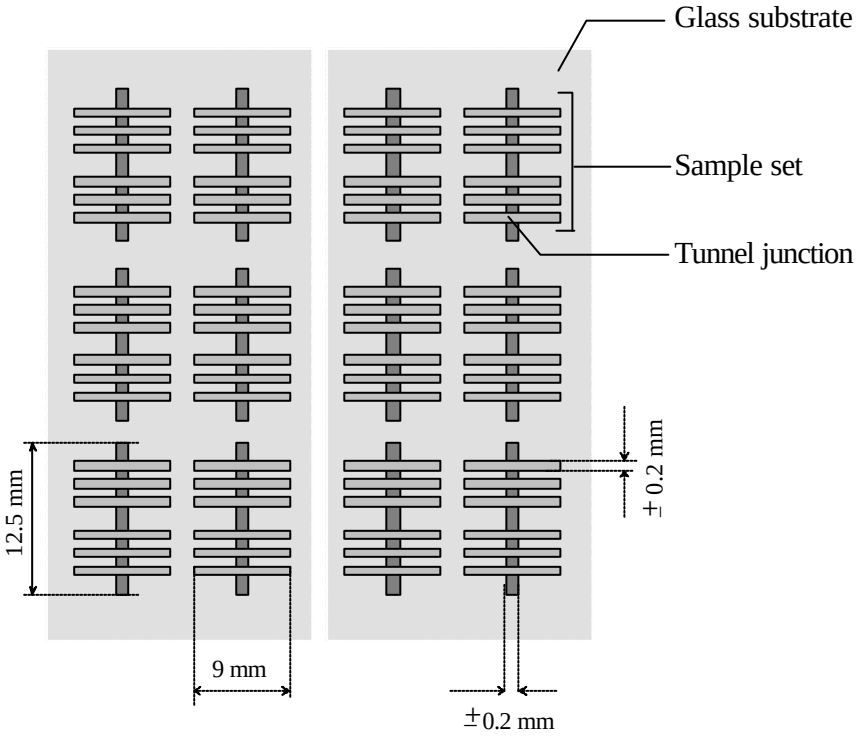

Figure 4.1 The final configuration of the deposited tunnel junctions. The drawing is not on scale.

To achieve a good attachment of the metallic electrodes to the substrate, sometimes a silicon seed layer is deposited onto the nitrogen cooled glass. Thereafter the bottom metallic electrode and the aluminium layer are evaporated through shadow masks while the glass substrate was still cooled to

increase the smoothness of the surface. The tunnel barrier is prepared by oxidation of an aluminium interlayer or an aluminium electrode at an ambient temperature of approximately 300 K in a glow discharge at an O_2 pressure of 70 mTorr. Finally the top electrode is deposited through a perpendicularly positioned shadow mask at ambient temperature. To define a uniform anisotropy of the electrodes, a field of approximately 100 Oe, parallel to the direction of the bottom electrode, was applied during the deposition of the ferromagnets.

After the preparation a final Al_2O_3 protection layer can be directly deposited by an e-gun at ambient temperature over the glass substrate. Figure 4.1 shows the final deposited tunnel junctions after one run. In total twelve sample sets are prepared where each sample set contains six junctions. The individual preparation steps for the different type of samples are described in detail below.

Preparation of $Al/Al_2O_3/Al$ nonmagnetic tunnel junctions

Figure 4.2 shows the preparation steps of nonmagnetic tunnel junctions. Only the preparation of one sample set, which contains six junctions, is shown. Chapter 5 will deal with the measurements of one junction of this set.

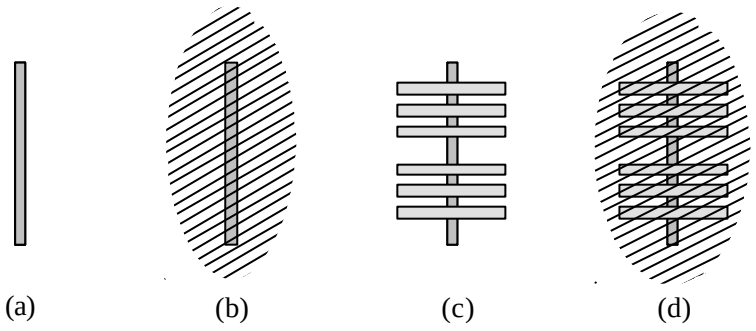

Figure 4.2 The preparation of a nonmagnetic aluminium junction. More details are described in the text. (a) Deposition of the Al bottom electrode. (b) Oxidation of the bottom electrode with a glow discharge. (c) Deposition of the Al top electrode. (d) Deposition of an Al_20_3 protection layer over the whole sample.

An aluminium strip with a thickness of 44 Å was deposited to form the bottom electrode (step a). Thereafter the sample gets oxidised for 45 s (step b). Subsequently aluminium top electrodes with a thickness of 100 Å were deposited (step c). Finally a 20 Å Al_2O_3 protection layer was deposited covering the whole sample (step d).

Figure 4.3 shows a scanning electron microscope picture of the prepared junctions. The width of the bottom electrode is 100 µm and the width of the top electrode is 200 µm, so the total area of the tunnel junction is $2 \cdot 10^{-4}$ cm^2.

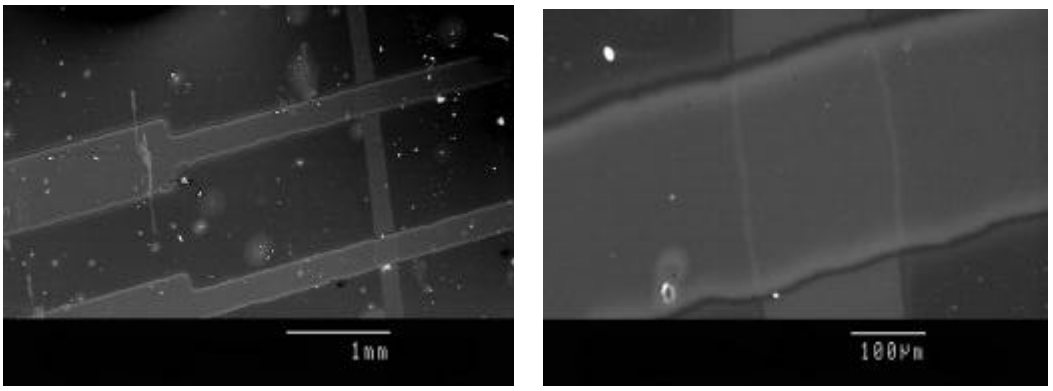

(a) *(b)*

Figure 4.3 Scanning electron microscope pictures of the prepared aluminium junctions. (a) Two tunnel junctions. (b) One junction zoomed in. The white spots on the pictures are due to small amounts of silverpaint, which was used to make electrical contacts on the electrodes.

Figure 4.4 shows a cross-section (not on scale) of the final deposited tunnel junctions. The junction has two aluminium electrodes and the potential barrier is the insulating aluminium oxide.

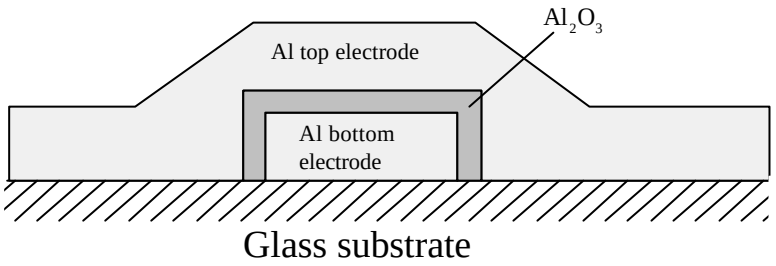

Figure 4.4 Cross-section of the nonmagnetic tunnel junction. The figure is not draw to scale.

Preparation of a $Co/Al_2O_3/NiFe$ magnetic tunnel junction

Figure 4.5 shows the different steps of the preparation of a $Co/Al_2O_3/NiFe$ magnetic tunnel junction. Only the preparation process of one sample set on the glass substrate is shown. Chapter 6 will deal with the measurements of one junction of this set.

Initially a 10 Å silicon seed layer was deposited. Subsequently, a 100 Å Co electrode was deposited in the form of a strip (step a). A layer of 12 Å aluminium was evaporated over the whole substrate, then the Al was oxidised for 100 s (step b). Thereafter defining Al_2O_3 layers with a thickness of 60 Å were deposited with a separate shadow mask (step c). These layers were directly deposited with an Al e-gun in an O_2 atmosphere. Since the defining layers have a thickness of 60 Å the electron tunnelling current is forced to flow only through the middle part of the underlying plasma oxidised Al layer, and not through the less defined edges of the structure. Next NiFe top electrodes with a thickness of 150 Å were deposited (step d), and finally, a 20 Å Al_2O_3 protection layer over the whole sample was deposited (step e) with an Al e-gun in an O_2 atmosphere. The total tunnelling area (not covered with the Al_2O_3 defining layer) of one junction is 200x750 µm, so the total area of the junction becomes $15 \cdot 10^{-4}$ cm^2.

Figure 4.6 shows a cross-section of the prepared final tunnel junction in which the role of the defining layer can be easily recognised.

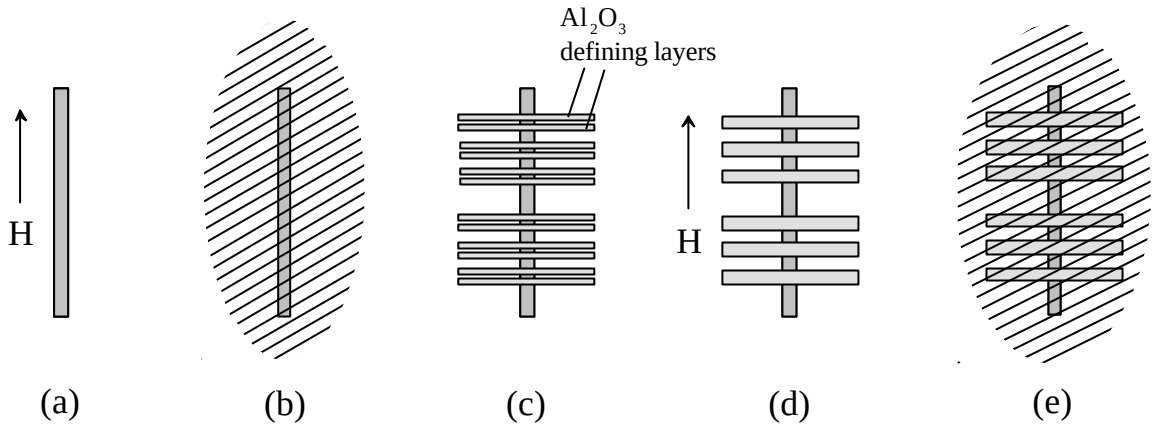

Figure 4.5 The preparation process of a magnetic tunnel junction. More details are given in the text. (a) Deposition of the Co bottom electrode. (b) Deposition of a thin aluminium layer and oxidation with a glow discharge. (c) Deposition of the Al_2O_3 defining layers. (d) Deposition of the NiFe top electrodes. (e) Deposition of an Al_2O_3 protection layer.

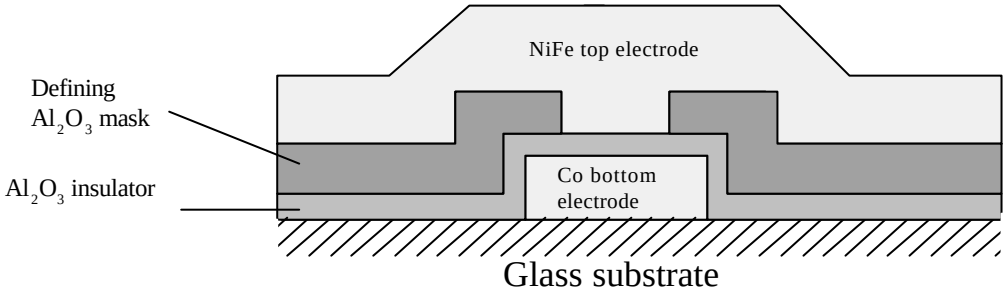

Figure 4.6 Cross section of the magnetic junction with defining mask. The figure is not draw to scale.

Preparation of series magnetic tunnel junctions with different oxidation times of the interlayer

A set of magnetic tunnel junctions was prepared where the oxidation time of a aluminium interlayer of the junction was varied between 30 s and 490 s. The different steps of the preparation of two sample sets are represented in figure 4.7. Chapter 7 will deal with the measurements made on this series of junctions with different oxidation times.

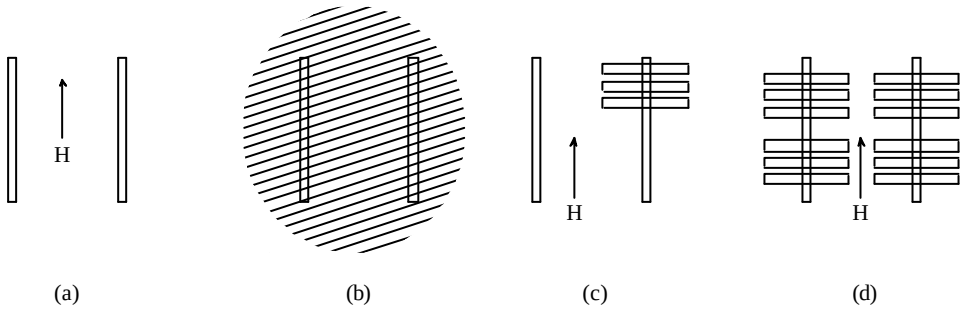

Figure 4.7 Steps of prepared magnetic junctions with different oxidation times. Step (a),(b),(c), and (d) are explained in the text.

First, a 10 Å silicon seed layer was deposited over the entire glass substrate, whereafter a Co electrode with a thickness of 80 Å was deposited (step a). An aluminium layer with a thickness of 12 Å was evaporated over the sample sets (step b). Next the samples became oxidised for 30 s, whereafter these tunnel junctions were completed by deposition of three 80 Å NiFe top electrodes (step c).

Subsequently the sample sets were oxidised again, now e.g. for 60 s, followed by deposition of another three electrodes. The total oxidation time of the Al interlayer of the three newly formed junctions is now 90 s. This process was repeated until 4 sets of junctions with different oxidation times of the interlayer were fabricated (step d). In two preparation runs, samples were prepared with oxidation times of the aluminium interlayer of 30, 60, 90, 120, 150, 210, 300 and 490 s. Finally a 20 Å Al_20_3 protection layer was deposited (with an Al e-gun in an O_2 atmosphere) covering the whole substrate. Figure 4.8 shows a cross section (not proportional) of one junction with a certain oxidation time. The width of the bottom electrode and the top electrode are 200 μm, so the total area of the tunnel junction is $4 \cdot 10^{-4}$ cm^2. It must be noted that inherent to the preparation method also the bottom and the top electrodes become partly oxidised.

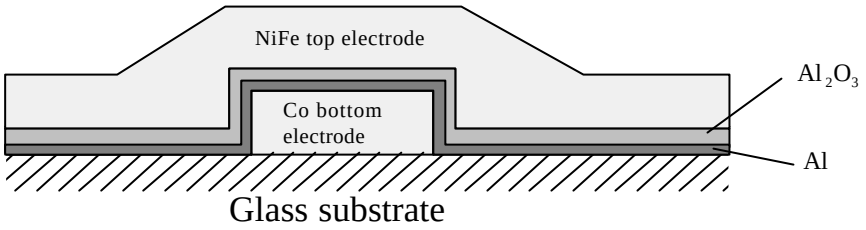

Figure 4.8 A cross section of a Co/Al/NiFe junction. The figure is not draw to scale.

4.2 Tunnel MagnetoResistance measurements

4.2.1 General

The basis resistance measurements on tunnel junctions are performed with a four-point contact method, as shown in figure 4.9. On one side of the top and the bottom electrode the current contacts, I+ and I-, are made to force the current to flow across the insulating barrier. On the other side of the electrodes the voltages V+ and V- are measured.

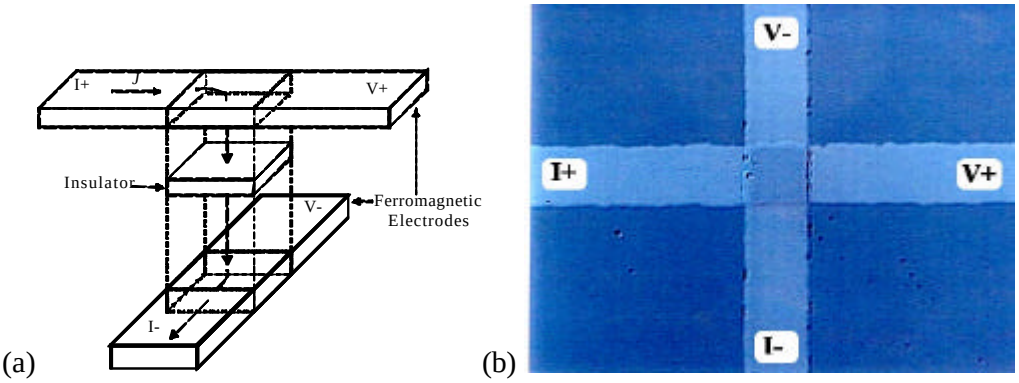

Figure 4.9 (a) Four point measurement on a tunnel junction. (b) SEM-photo of a junction prepared at Philips Research Laboratories with the configuration of the electrical contacts indicated.

Figure 4.10 shows a schematic view of the tunnel MagnetoResistance (MR-) equipment available at the Eindhoven University of which a short description will follow below. More details of the equipment and performances can be found in references [26-27]. The total equipment is more sophisticated than shown in the figure, and is also used to perform other type of measurements. The MagnetoResistance equipment performs three types of measurements: (1) The resistance as a function of the magnetic field (*RB-measurements*), (2) the resistance as a function of the temperature (*RT-measurements*) and (3) the voltages as a function of the applied dc-current density (because theoretical models describe the current as a function the voltage, in this report these measurements are called *JV-measurements*).

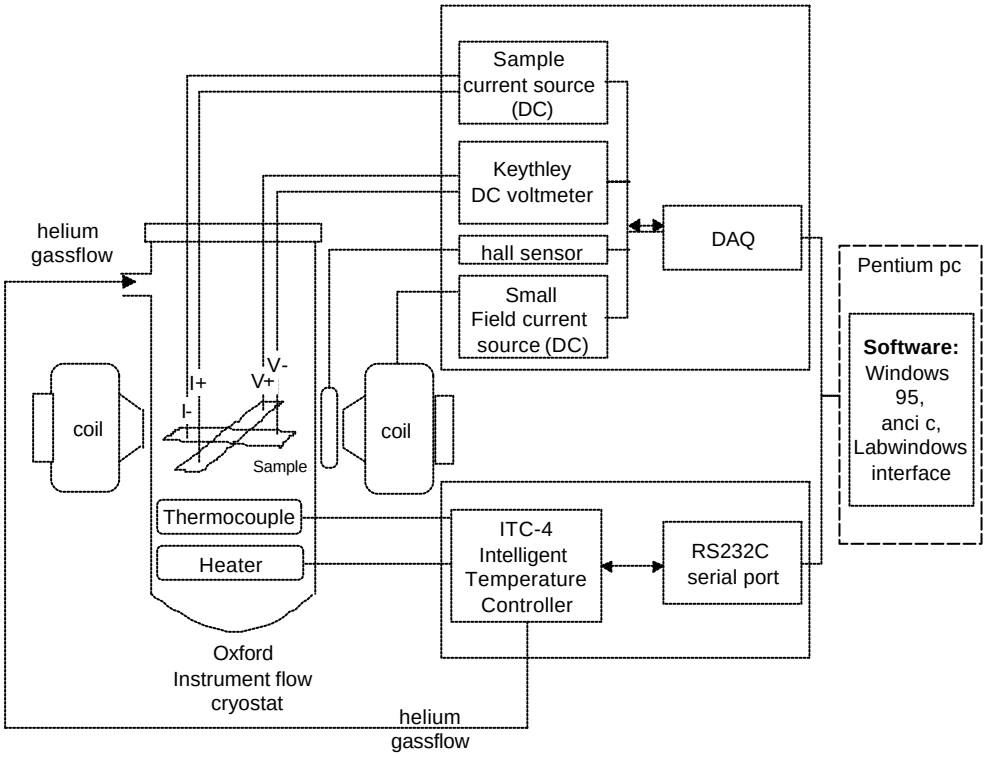

Figure 4.10 Schematic overview of the equipment used to measure tunnel junctions. The total equipment is more sophisticated and is also used to measure GMR and AMR of multilayers and granular systems. The components are further explained in the text.

To measure the resistance of a junction a dc-current from I+ to I- can be set by a home-build current source in ranges of 100 mA, 10 mA, 1 mA, 100 µA, 10 µA and 1 µA. Within one range 4096 equal

steps can be made. The maximal absolute error of the current-source is approximately 0.53% of the range of the current-source. The dc-voltage is measured by a Keithley 1282 sensitive digital voltmeter. The Keithley has five voltage-ranges: 3 mV, 30 mV, 300 mV, 3V and 30 V. The maximal error of the ADC and Keithley is 0.1% of the used range. For more information about the current-source and the Keithley voltmeter implemented in the MR-equipment see the report of Hoefnagels [27].

The sample is contacted to a sample holder which is placed in an Oxford Instrument flow cryostat (see figure 4.10). The temperature of the sample is measured with a thermocouple and controlled by an Intelligent Temperature Controller (ITC-4). The sample can be cooled by liquid helium and warmed up by a heater within a range of approximately 4 K to 350 K. The cryostat is placed between the coils of an electromagnet (see figure 4.10). Although the magnetic induction can be swept between -1.25 T and 1.25 T, for tunnel resistance measurements a lower field is used between -125 mT and 125 mT with a minimum step size of 0.04 mT. A home-build dc-current source sets the magnetic field, which is measured by a Hall-sensor. The smallest field step that can be measured by the hall sensor is 0.4 Oe, the maximum offset of a field-measurement is 1 Oe and the maximal relative error made is 1.7% of the field.

A Pentium 100 MHz, working with the operating system Windows95, controls the equipment. An RS232C serial port connects the Oxford Intelligent Temperature Controller. A Data Acquisition card (DAQ) connects (1) the dc-current source which sets a current to the sample, (2) a voltmeter, (3) the Hall sensor and (4) the dc-current source which sets a current for the magnetic field coils. To perform measurements a C based program is written in the graphical orientated interface of Labwindows, National Instruments Corporation.

4.2.2 Improvements

There were several improvements that had to be made before the MR-equipment was suitable to measure tunnel junctions. Before this research project started, the RB-measurements were still made with a 286 computer working with a PhyDAS data acquisition system. RT- and JV-measurements were already performed on a Pentium 100 MHz computer with a Data Acquisition Card and a program written in LabWindows.

In this graduation project, the RB-measurement was implemented in the LabWindows program on the Pentium, to improve the equipment towards a stand-alone system. A concept-version of the RB-measurement in Labwindows was already written by P. Soetens [26], but this had to be completed and improved to work correctly. Furthermore, a new switch was installed, which can be controlled by the DAQ. This switch turns the polar direction of the current which set the magnetic field. After the installation of the hard and software, the Hall probe, which measures the magnetic field, was calibrated. Also the overall program was tested, the program structure and the DAQ-output ports were made more logical and the interface was improved. More configuration data are stored into the data files, so it is now possible to load an old measurement with all system settings.

4.2.3 New tunnel junction contact-device

In this research project a device was developed to contact junctions with needle spring probes. The contact device is connected to the end of a sample holder rod, which is an insert that can be put into the cryostat. The device is shown schematically in figure 4.11a. Inside the device wires to the probes are soldered to connect the spring probes. In the figure only one wire and one spring probe is shown. The sample, with a set of six junctions on it, is connected to the device by a small plate below the sample (see figure 4.11a). The construction drawings of the contact device and the sample holder rod are given in appendix H.

Figure 4.11b schematically shows a sample set with 6 tunnel junctions, which is the junction configuration used at MIT. The positions of all needle connections are shown as black dots. As can be seen, fourteen spring probes are implemented in the device, to connect all six junctions. Although still only one junction at the time can be measured, this device has an advantage over silver paint contacts (contacting wires directly to the electrodes by conductive silverpaint); contacting with spring probes is quicker and it is also possible to switch the measurement to an other junction on the set, without taking the sample holder out of the cryostat.

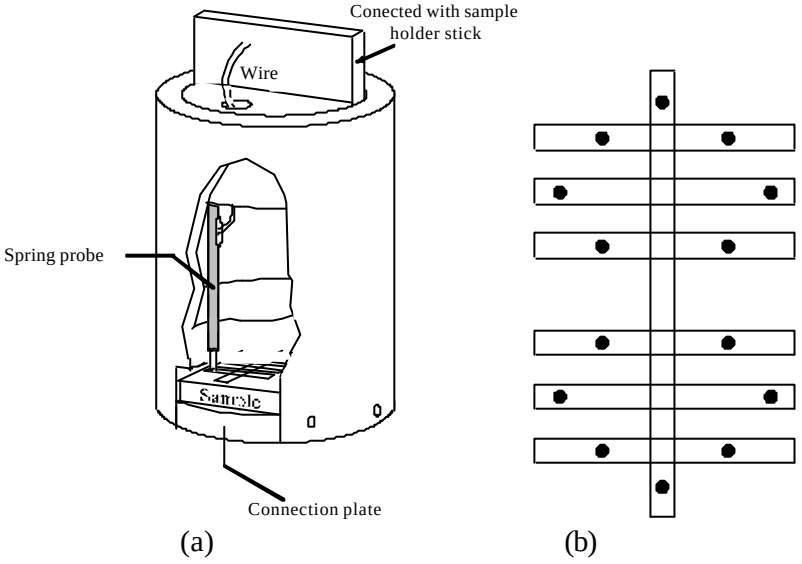

Figure 4.11 (a) Schematic drawing of the junction contact device. The junctions are connected with spring probes. In this figure only one spring probe, with one wire, is shown. The actual height of the device is 27 mm and the diameter is 19 mm. (b) A sample set with six junctions (not in scale). The spring contact positions on the electrodes are shown. To contact all electrodes the total devices consists of 14 probes.

4.2.4 How to measure tunnel junctions?

Tunnel junctions are sensitive electronic components. Electric measurements can cause a breakdown, after which the junctions get an ohmic linear JV-characteristic with a resistance lower than 100 Ω. For the experiments described in this report a save voltage range to measure is an absolute maximum of 0.6 V. Peak voltages higher than 0.6 V can be fatal for the junctions. More information about breakdown of tunnel junctions can be found in reference [28] and [29]. To prevent peak voltages, switching on or off electrical equipment, such as computer and lights, should be avoided during the time the junction is contacted. The old MR-program switches the current through the sample on before, and off, after every individual RT- and RB-measurement, which also gave rise to peak-

voltages. To prevent those peak-voltages a new option in the MR-program is implemented which keeps a constant current on the junction, while a sequence of RT- and/or RB-measurements can be made. It is also important to make good electrical contact onto the electrodes. If a contact turns loose, the current source builds up a high voltage. If small vibrations cause the electrode to make contact again, this will give a high voltage-drop over the junction, which can be fatal.

Beside the chance of breakdown due to peak voltages another aspect to take care of is the light sensitivity of the tunnel junctions. Light causes a voltage drop over the junction. Since the sample is measured in the cryostat were it is dark, this effect is not measured in the experiments.

4.3 Magnetic characterisation with MOKE measurements

MOKE measurements are performed to characterise the magnetic properties (e.g. the coercive field) of the junction and the electrodes qualitatively. The magneto-optical Kerr effect is the phenomenon that the polarisation state of light incident on the surface of magnetic materials changes after reflection. Coherent light is emitted by a He-Ne laser and is focussed to a spot size of approximately 50 µm which makes it possible to characterise the magnetic properties at the position of the junctions. The light has a typical penetration depth of approximately 30 nm in a metal film. The magnetic induction used to measure a tunnel junction can be varied between -400 Oe and 400 Oe with a maximum accuracy of 0.1 Oe. For more information about the method of MOKE measurement and the application to magnetic tunnel junctions, see references [30-32].

5 Results for a nonmagnetic junction

The electric characteristics of a nonmagnetic tunnel junction will be presented in this chapter. This junction has a 44 Å aluminium bottom electrode, which was oxidised for 45 s, and a top electrode of 100 Å. The junction is prepared as described in the experimental set-up, section 4.2. In the first section of this chapter JV-measurements at different temperatures and the extracted barrier parameters will be presented. The next section will deal with the temperature dependence of the junction resistance and will be compared with theoretical predictions.

5.1 Current as a function of the applied voltage and extracted barrier parameters

Figure 5.1 shows the current as a function of the applied voltage (JV) performed with current intervals of *DI*=2 μA on the nonmagnetic junction at temperatures in the range of 5 K to 305 K. Also measurements at 50 K and 100 K are made, but these are not shown in the figure because they visually overlap with the measurement at 5 K. To start with, it is observed that the JV-measurements have the same curvature as derived theoretically in chapter 2 (see figure 2.4c). This effect is caused by the decrease of the mean barrier height as the applied bias voltage increases.

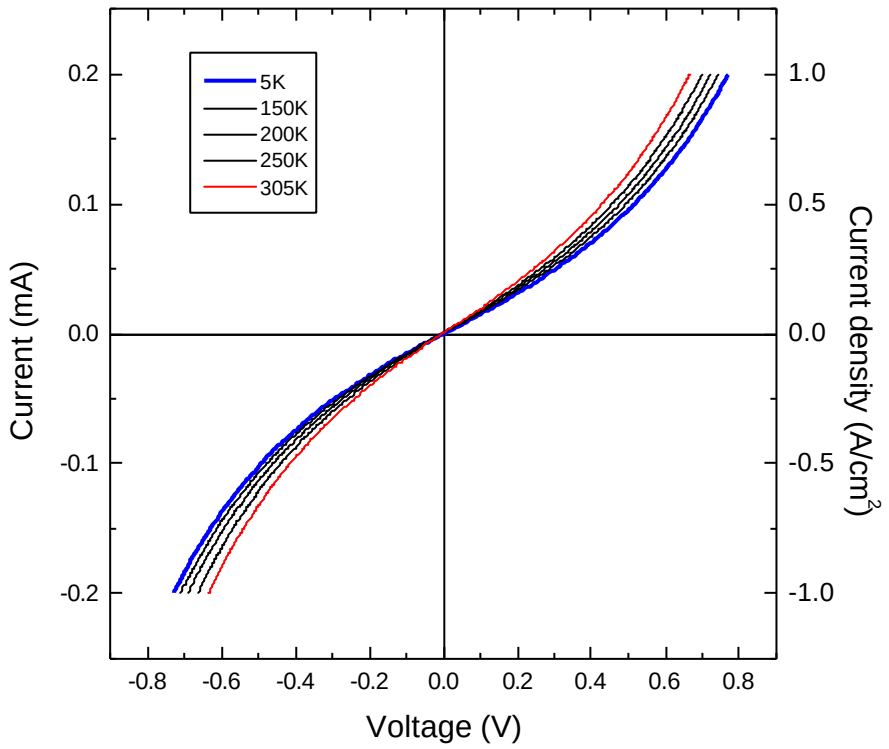

Figure 5.1 JV-measurements on a Al(44 Å)/Al_2O_3(45 s oxidised)/Al(100 Å) junction at different temperatures within the range of 5 K to 305 K. Also measurements at 50 K and 100 K are performed, but these are not shown because they overlap with the measurement at 5 K on this scale.

For all applied voltages the current density increases (the resistance decreases) as the temperature rises. It is possible that this effect is related to the increase of the occupied states with an energy above the Fermi level as described in chapter 2, section 2.3.4. Another reason for this effect may be the increase may be the spin-independent factor G_{SI}, see section 3.2. We will return to this in section 5.2.

The barrier parameters of the Al_2O_3 interlayer can be extracted from JV-measurements by finding the appropriate parameters for the functions of Simmons (2.27) or Brinkman (2.38) by a numerical fit to the JV-measurements. An example of a JV-measurement at 5 K, within a range of 600 mV, and the functions of Simmons and Brinkman derived for zero Kelvin, are shown in figure 5.2, together with the parameters found by the numerical fit.

It should be noted that the extracted barrier parameters differ as the voltage range used in the fit of the JV-measurement gets smaller, see appendix F. To take whole the measurement in to account, the functions of Simmons and Brinkman was fitted into the measurement range of 600 mV, yielding the extracted barrier width s and barrier height p reliably within 15%. The extracted barrier asymmetry delta Δp is however far less reliable and can deviate more than 50 %.

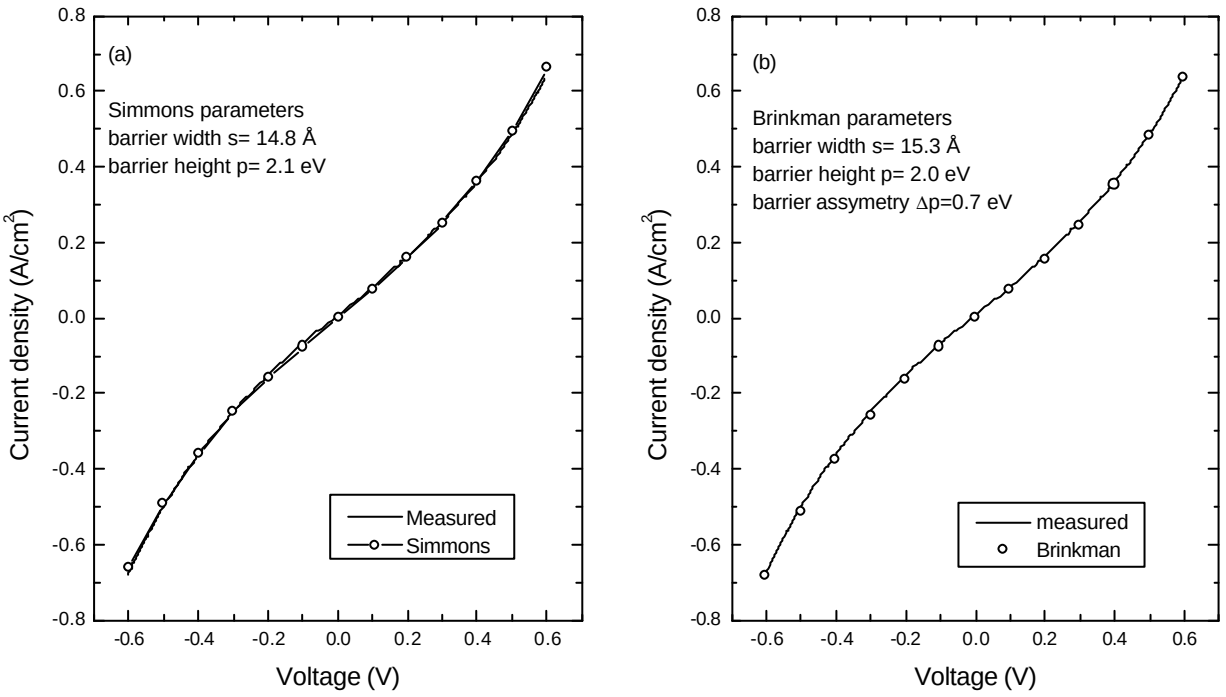

Figure 5.2 An example of a JV-measurement at 5 K on a Al(44 Å)/Al_2O_3(45 s oxidised)/Al(100 Å) junction compared with the function of Simmons (a) and Brinkman (b) with the appropriate parameters.

The barrier parameters of Simmons are indicated in figure 5.2, and are s≈15 Å, p≈2.0 eV. For these junctions it is difficult to verify the extracted barrier thickness, but we will return to this in the following chapter. The extracted barrier height of 2.0 eV correspondence with the barrier height founded by Nelson et al. [13]. They analysed the potential barrier of a thin anodically formed Al_2O_3 film by photoemission, and also found a barrier height of 2.0 eV.

Due to an asymmetry in the JV-measurements, the Simmons function does not fit correctly, as one may easily observe upon a closer inspection of figure 5.2. The asymmetry in the JV-measurement is caused by a barrier asymmetry of $Dp \approx 0.7$ eV, a value extracted from fitting with the formula of Brinkman. It is possible that the barrier asymmetry results from a gradient in the Al/Al_2O_3 ratio across the barrier induced by the method of oxidation, which is also mentioned in reference [13].

Although the functions of Simmons and Brinkman are derived for zero Kelvin the barrier parameters were also extracted from JV-measurements at higher temperatures. Figure 5.3 shows that the extracted barrier width *s* (figure 5.3a) and barrier height p (figure 5.3b) are only slightly dependent of the temperature. In contrast, the JV-measurements differ significantly as a function of T as shown in figure 5.1. The reason for this fact is that only exponential changes in the JV-characteristics should give rise to a considerable differences in *s* and/or *p* of Simmons and Brinkman theory, due to the exponential decrease of the resistance with the barrier parameters, see equation (2.27) and equation (2.38). The temperature dependence of *Dp* at high temperatures is not understood and may be due to the experimental error e.g. induced by the fitting procedure.

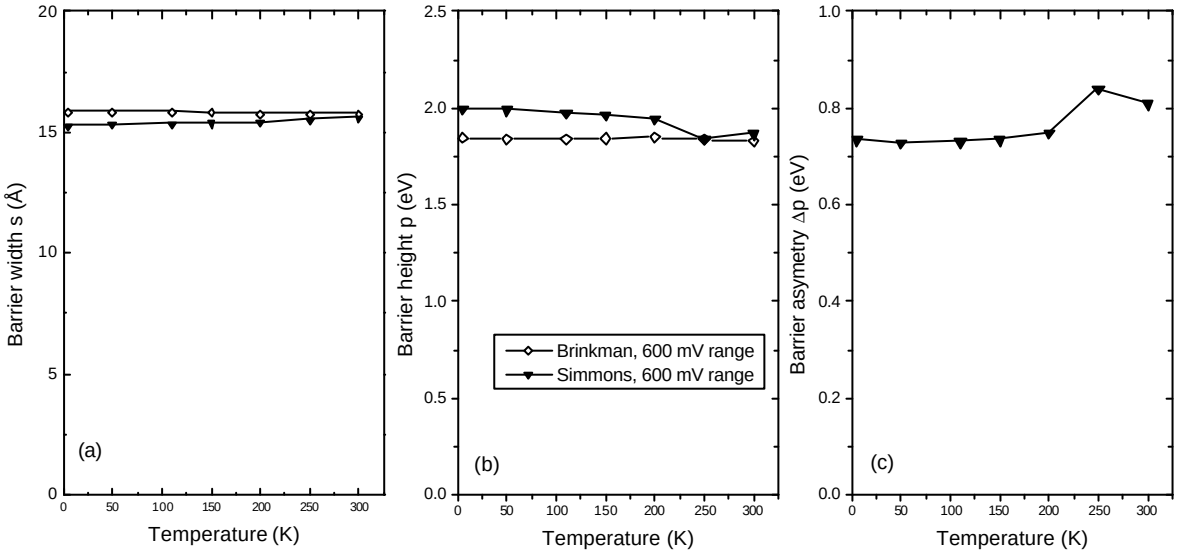

Figure 5.3 Fit results as a function of temperature. (a) The barrier width s, (b) the barrier height p, (c) the barrier asymmetry Dp.

To compare the functions of Simmons and Brinkman with the JV-measurements in more detail, one has to consider also the conductivity, dJ/dV. Brinkmans expression of the conductivity (equation 2.36) is parabolic. The conductivity of Simmons, calculated by differentiation of the JV-function of Simmons with the barrier parameters p=15 eV and s=2 eV as indicated by experiment, is shown in figure 5.4, and is parabolic as well.

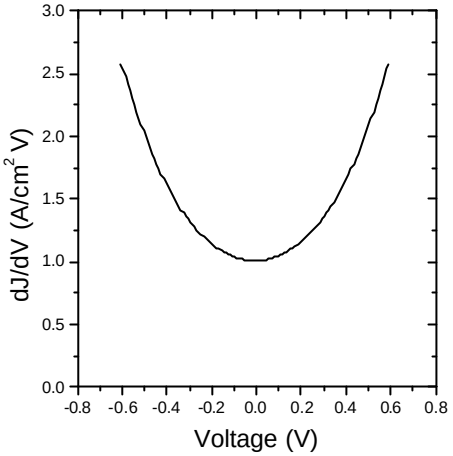

Figure 5.4 The conductivity (dJ/dV), derived from the Simmons equation with the barrier height p=2 eV and the barrier width s=15 Å.

Figure 5.5 shows the conductivity (dJ/dV) derived from the JV-measurements made within the temperature range of 5 K to 305 K (the JV-measurements are shown in figure 5.1). The numerical derivations are made by an algorithm which is implemented in the software program Origin 4.0, Microcal Software, Inc. This algorithm uses a smoothing method, in this case of 13 measure points, that performs a local polynomial regression around a certain measurement. The derivates calculated are the coefficients of the local polynomials.

The derived conductivity from the measurements as a function of the voltage is reasonably parabolic. Only at zero-bias the conductivity curve has a small dip. Neither Simmons nor Brinkman predicts this feature at zero voltage, and needs further (theoretical) investigation.

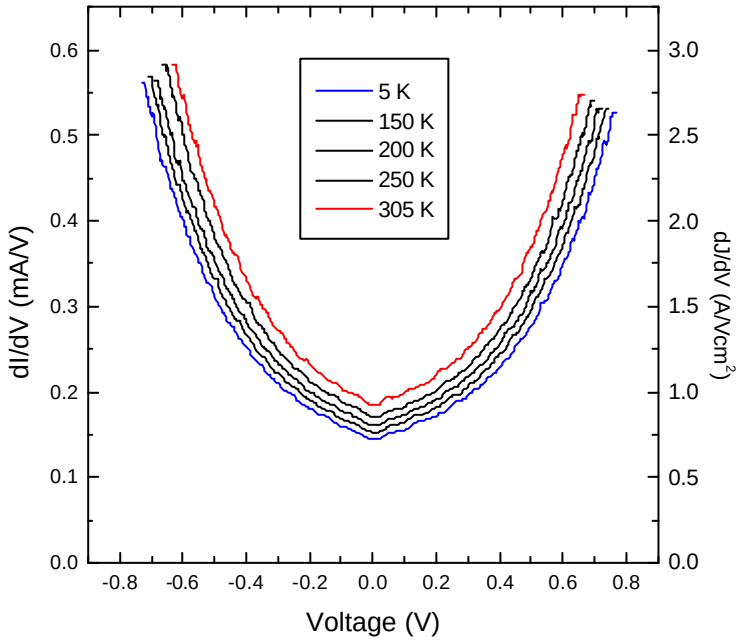

Figure 5.5 The numerical derived conductivity dJ/dV from the experimental JV-curves on a Al(44 Å)/Al_2O_3(45 s oxidised)/Al(100 Å) junction at different temperatures.

5.2 Resistance as a function of temperature; comparison with theory

The solid line in figure 5.6 shows the resistance as a function of temperature (RT) which is made with a constant current of 10 μA (current density of 2.5 mA/cm^2) whereas the applied voltage was approximately 70 mV. In section 2.3.4 the RT-dependence has been calculated based on the thermal occupation of the energies above the Fermi-level. The theoretical RT-dependence is shown by the dotted line in figure 5.6 and is calculated with the parameters extracted from the JV-curves in the previous section: $s \cong 15$ Å and $p \cong 2$ eV. For the calculated RT-characteristic, R(J,0) is pinned to the measured resistance at 5 K, to ease the comparison. It can be seen that the theoretical RT-characteristic deviates significantly from the experimental data. If one defines $DR = R_{5\,K} - R_{275\,K}$, the theoretical $DR/R_{0\,K} = 2.7\,\%$ and the measured $DR/R_{5\,K} = 18.1\%$, a similar value were also noted by Chang et al. [11].

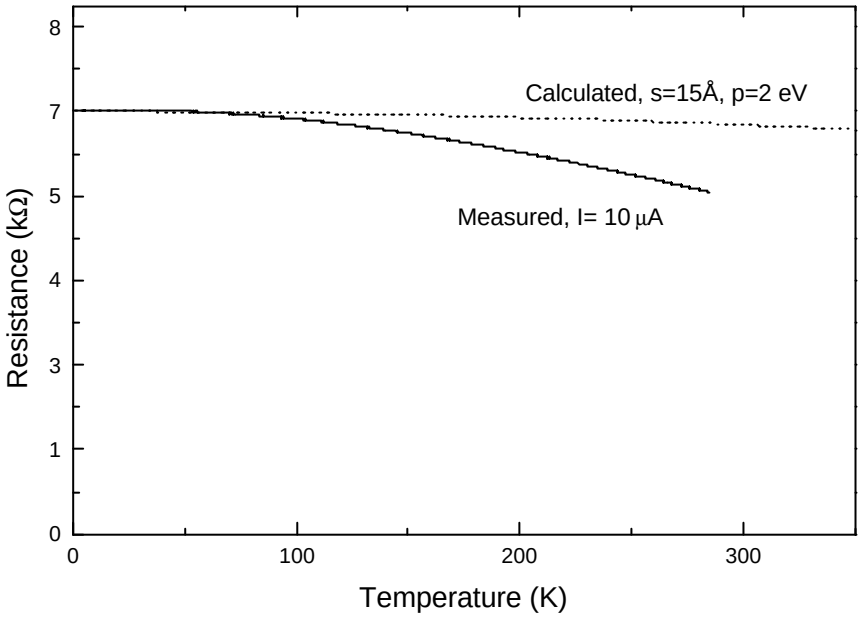

Figure 5.6 Resistance as a function of the temperature. Straight line: RT-measurements at I=10 mA. Dotted line: calculated RT-curve by the equation of Simmons.

An alternative explanation for the behaviour of the resistance can be found in the temperature dependence of the spin independent conductivity G_{SI} as recently suggested by Chang et al. [11], see section 3.2. This spin independent conductivity can be calculated by equation (3.10):

$$G_{SI} = \langle G \rangle - G_{T,} \tag{5.1}$$

where G_T is the elastic conductivity as given in section 2.3.4. Because for a nonmagnetic junction $P_1 = P_2 = 0$. This formula than becomes:

$$G_{SI} = G - G_T. \tag{5.2}$$

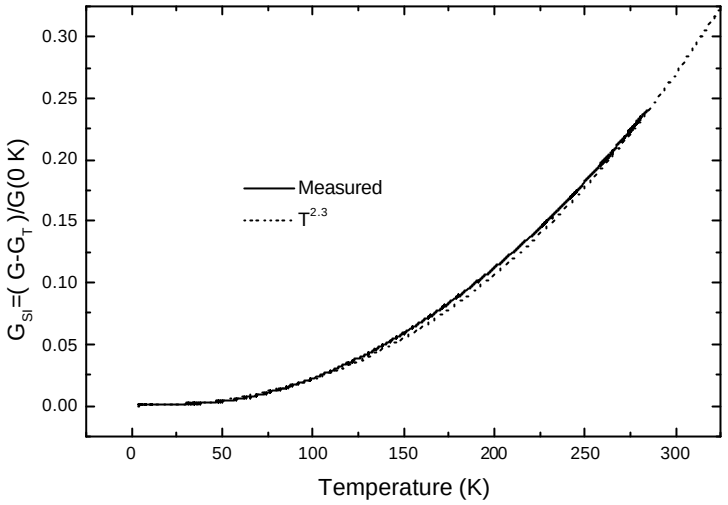

Figure 5.7 Measured spin independent conductivity G_{SI} compared with a function $G_{SI}\mu\ T^{2.3\pm0.1}$.

In figure 5.7 G_{SI} derived from the measurements is given where G is normalised to $G(0\ \mathrm{K})=1$. G_{SI} is found to be reasonably will described with a power law in T: $G_{SI}(T)\mu T^{2.3\ \pm0.1}$. This could indicate a thermal conductivity with two inelastic hops ($N=2$), as described in section 3.2, where theoretically $G_{SI}\mu T^{2½}$. Chang et al.[11] found a power law of $G_{SI}\mu T^{1.35\pm0.15}$ for a magnetic Co/Al_2O_3/Co junction.

6 Results for a magnetic tunnel junction

This chapter deals with experimental results of magnetic tunnel junction. The bottom electrode of this junction is made of Co and has a thickness of 80 Å and the top electrode is made of NiFe and has a thickness of 150 Å. The junction has a 14 Å Al-interlayer which is oxidised for 100 seconds. The preparation process of this sample is described in section 4.2.

The first section will deal with the basic characteristics of a magnetic tunnel junction. In the next section we will focus on the magnetic coupling of the magnetic layers across the insulating barrier.

6.1 Tunnel MagnetoResistance measurements

Figure 6.1 shows an example of a measurement of the resistance as function of the magnetic field (RB-measurement), where the magnetisation direction of the bottom and the top electrode are indicated by the arrows in black and grey, respectively. This measurement starts at a high negative field, beyond the coercive field of the electrodes (a). The magnetisation directions of both electrodes are saturated and aligned in the field direction. Because of the parallel alignment the resistance is low, see equation (3.3). As the field increases and changes sign, the magnetisation of the top electrode (arrow in grey) with the lowest coercive H_c changes its magnetisation direction, whereas the magnetisation of the other electrode (the arrow in black) remains the same (b). In this field range the electrodes are antiparallel aligned and as a result the junction resistance is high, see again equation (3.3). Upon raising the field further, the magnetisation direction of the other electrode also reverses, and becomes parallel to the other electrode at the field (c), corresponding again with a lower junction resistance.

An analogue process as described above occurs upon decreasing the magnetic field; first the alignment is parallel, then the alignment becomes antiparallel when the top electrode (in grey) changes its orientation (d) and finally again parallel, at a large enough negative magnetic field where the field sweep has been started (a).

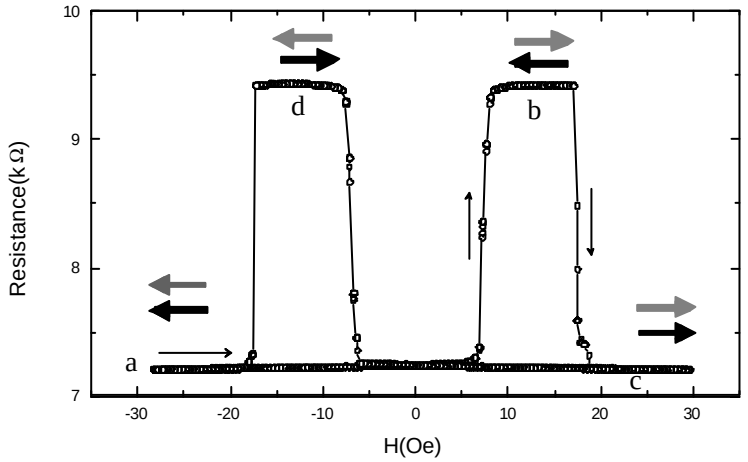

Figure 3.3 An example of a RB-measurement at 10 K. During the measurements a complete sweep of the field is performed. The alignment of the upper and lower layer is shown in the figure corresponding to the arrows.

In the next subsections, we will focus in more detail on the following subjects:

- Measurements of the resistance as a function of the magnetic field (RB-measurements).
- Measurements of the current as a function of the applied voltage (JV-measurements).
- Resistance as a function of the temperature (RT-measurements).
- The Junction MagnetoResistance (JMR) as a function of the temperature.

6.1.1 Resistance as a function of the magnetic field

The measurements of the resistance as a function of the temperature were performed at temperatures of 10 K, 50 K, 100 K, 150 K, 200 K, 250 K and 300 K and with a current of 1 μA. Four of these measurements are shown in figure 6.1. It can be seen that both the JMR and resistance decrease as the temperature increases.

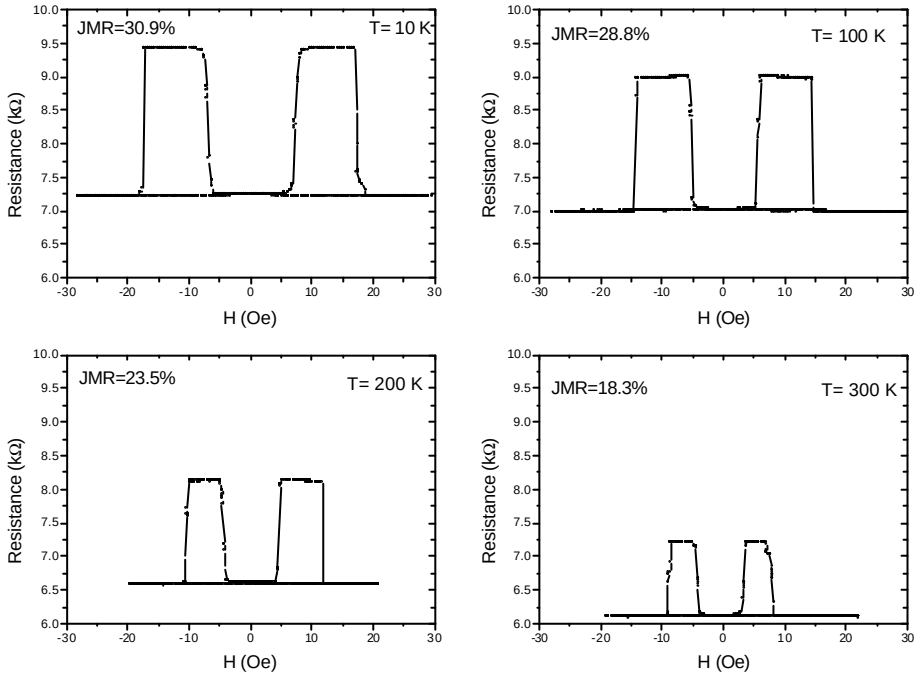

Figure 6.1 RB-measurements at different temperatures.

We like to mention that at all temperatures the resistance between the parallel and antiparallel alignment changes very abruptly, within a field range of about 1 Oe. Moreover the resistance in the antiparallel and parallel alignment are well defined resistance values, without any significant rounding as a function of the field. This excellent switching property is caused by the defining mask, which (as described in the experimental set-up) leads the current only trough the middle of a junction. As a consequence, edge effects of the magnetic clusters in the electrode are not taken into account if the junction resistance is measured. Two edge effects are possible: (1) The magnetisation direction at the edge is different as compared to the middle of the electrode. (2) The surface of the magnetic clusters at the edges is rougher than in the middle due to the shadow masks and therefore has a different magnetisation behaviour. Other measurements with no defining mask do not have such RB-characteristic, see e.g. figure 7.3 in the next chapter.

The end of this section will deal with the magnitude of the JMR as a function of the temperature in more detail, which we did not consider in this subsection.

6.1.2 Current as a function of applied voltage

Current-Voltage (JV)-measurements were performed in the parallel and in the anti-parallel alignments of the electrodes, where for the parallel alignment a field of -90 Oe was set and for the antiparallel alignment a field of H =0 Oe was set. Figure 6.2 shows the JV-measurements made at temperatures of 10 K, 150 K, 200 K, 250 K and 300 K. Also measurements at 50 K and 100 K were made, but, because in the figure they visually overlap with the measurements of 10 K, these measurements are not shown. The JV-measurements were performed with small current intervals of DI=0.5 μA within a range of 90 μA. The JV-measurements shows the same curved characteristics as also seen in the measurements on the nonmagnetic junction described in the previous chapter.

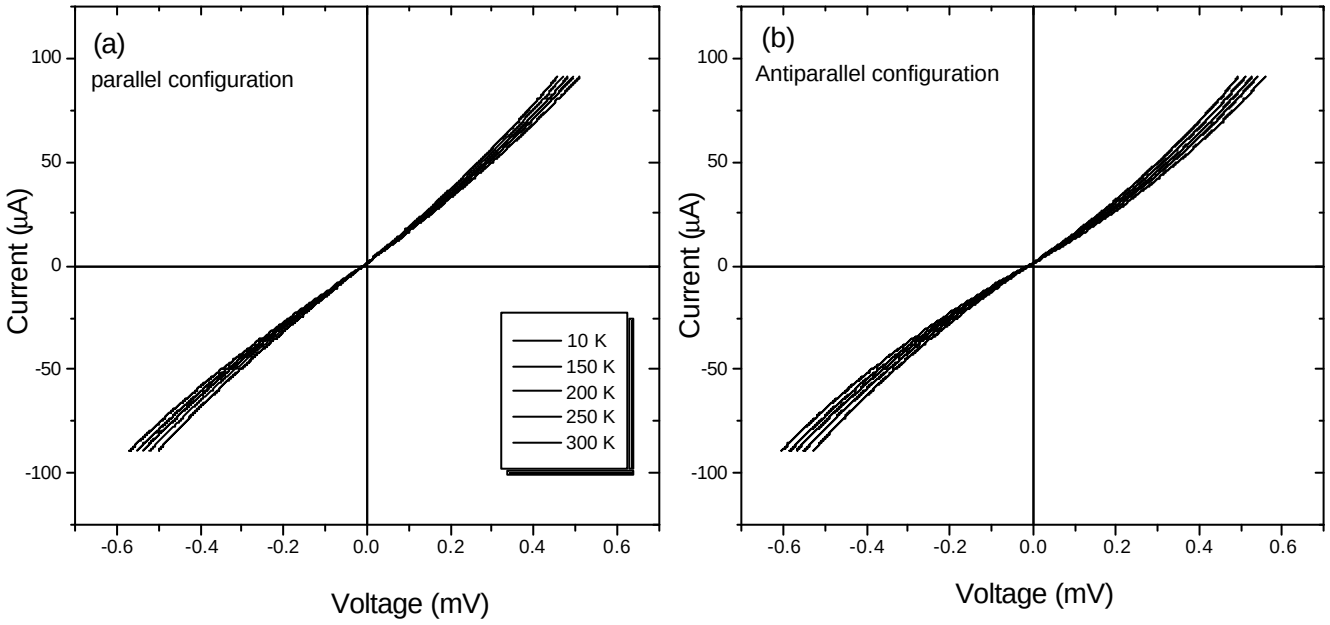

Figure 6.2 JV measurements in the parallel (a) and in the anti-parallel (b) alignments of the magnetic layers.

In the description of these curves we should in principle take into account the splitting between the electron bands between spin up and spin down, which is not addressed in the calculation of Simmons and Brinkman for nonmagnetic junctions. Despite this, barrier parameters of the Simmons equation (2.27) and Brinkman equation (2.38) are extracted by a numerical fit to the JV-measurements. Figure 6.3a gives an example of a Simmons function found at 10 K, where the magnetic moment of the electrodes are parallel aligned. The extracted fit parameters are a barrier width s=9.4 Å and a barrier height of p=3.4 eV.

Like in the previous chapter, again it is difficult to verify how the extracted barrier thickness compares with the actual barrier thickness, although it agrees reasonably well with the initial Al thickness of 14 Å. The extracted barrier height of 3.4 eV is larger than founded with photoemission measurements

by Nelson et al. [13] for an $Al/Al_2O_3/Al$ junction (which was 2.0 eV). No literature was found in which the barrier height of Co or NiFe (metals of the electrodes) was measured by this method.

The formula of Simmons does not correctly fit with the measurement, as can be judged in figure 6.3a. It appears that the junction has an asymmetric barrier potential of Dp=-2.6 eV, a value extracted by a numerical fit of the formula of Brinkman to the JV-measurement of 10 K in the parallel alignment of the electrodes. This barrier asymmetry is almost the same as the extracted barrier height itself, which is a very doubtful result. The barrier asymmetry may be caused by the difference in workfunctions of Co and NiFe (see section 2.2). A part of it can also be caused by an asymmetric Al_2O_3 barrier, due to composition gradients induced by the method of oxidation (an oxygen glow discharge).

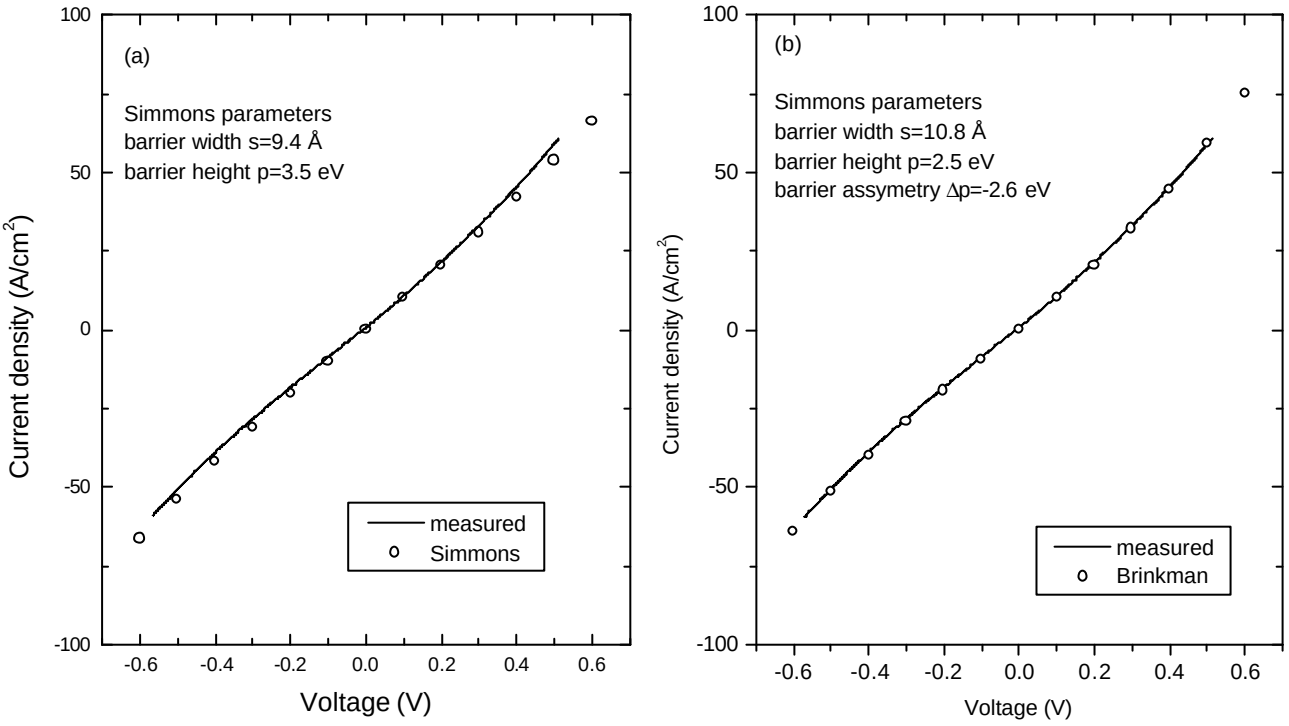

Figure 6.3 Example of a JV-measurement at a Co(80 Å)/Al_2O_3/NiFe(150 Å) junction at 10 K with the electrodes in the parallel alignment. (a) With a Simmons function and (b) with a Brinkman function found from a numerical fit to the JV-measurements.

Although the function of Simmons and Brinkman are derived for zero Kelvin, the barrier parameters were also extracted from JV-measurements at higher temperatures with a numerical fit to those functions. The extracted barrier parameters are plotted as a function of the temperature in figure 6.4 and it follows that the barrier width is s=11.6±1 Å, the barrier height is p=2.2±0.3 eV and the barrier asymmetry potential is Dp=-0.6±0.3 eV, when one would rely on Brinkman's model. It is also seen that these parameters strongly depend on the orientation of the magnetisation which is, as we mentioned before, due to the neglect of the magnetic characters of the electrodes.

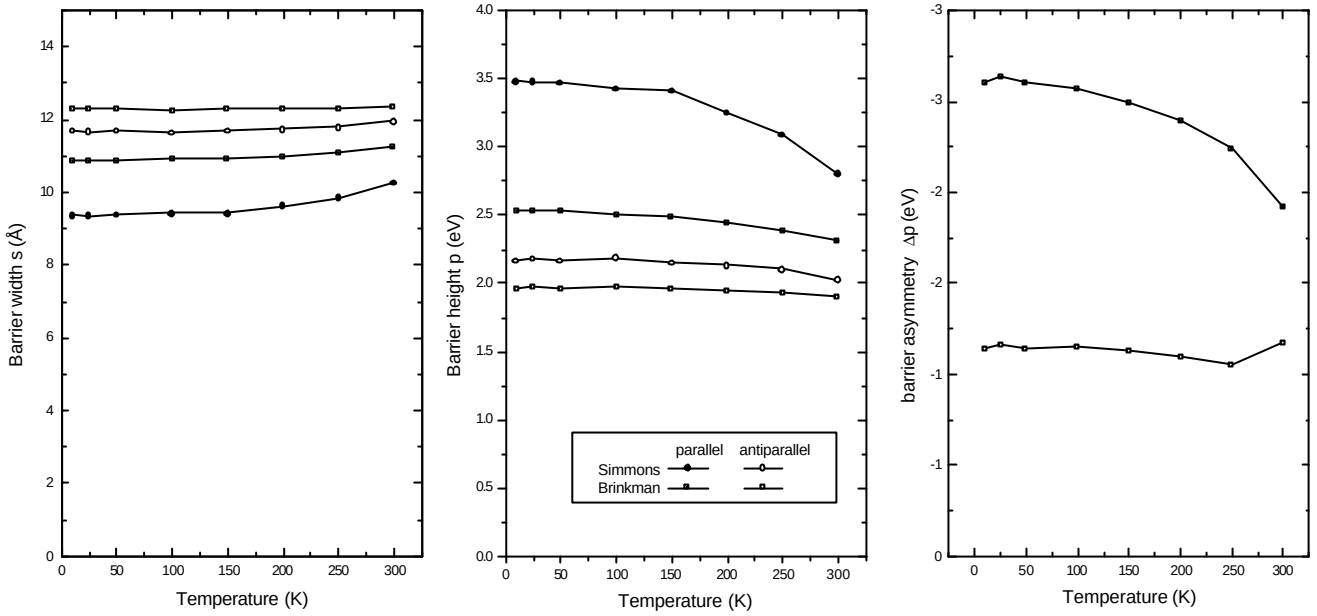

Figure 6.4 Barrier parameters extracted from the JV-measurements at different temperatures in the parallel and antiparallel configuration. The barrier width s; the barrier height p; the barrier asymmetry Δp.

Similar to the conclusions from the measurements of the nonmagnetic junctions in chapter 5, also for a magnetic junction the extracted barrier parameters *s* and *p* are only slightly temperature dependent, except for the parameters from Simmons formula in the parallel alignment, which can be caused by a temperature dependent barrier asymmetry, as seen in the right part of figure 6.4. The reason for this rather large T-dependence is not clear.

In more detail the theoretical functions of Simmons and Brinkman can be compared with the measurements by considering the conductance, dJ/dV, as a function of the voltage. From chapter 5 it was concluded that both the functions of Simmons and Brinkman have a parabolic form. Figure 6.5 shows the numerical derived conductance, dJ/dV, as a function of the applied voltage. As compared to the nonmagnetic measurements of the previous chapter both conductivities are less parabolic, so the current density formulas of Simmons and Brinkman deviate more from the measurements. This was expected by additional effect in magnetic junctions, such as the different workfunctions of Co and NiFe, the different wave vectors at the Fermi level and the summation of two currents, one for spin up and one for spin down electrons (see section 3.1). As a consequence the formulas of Brinkman and Simmons seem to be less suitable to extract barrier parameters from JV-measurements.

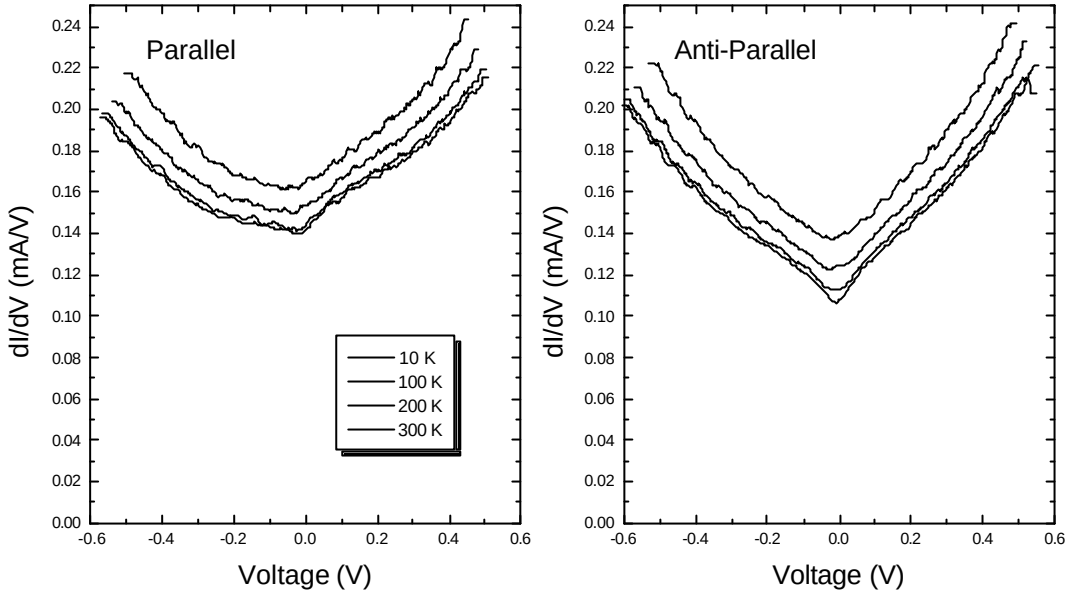

Figure 6.5 The conductivity of the parallel and the antiparallel alignment as a function of the applied voltage.

6.1.3 Temperature dependence of the resistance

Figure 6.6 shows a measurement of the resistance as function of the temperature (RT-measurement) in the parallel and in the antiparallel situation. The parallel RT measurement is performed with a field of –90 Oe and the antiparallel measurement is performed with a field of H=0 Oe. Also the resistances extracted from the RB-measurements are shown as scattered data points to show the consistency with the RT-measurements.

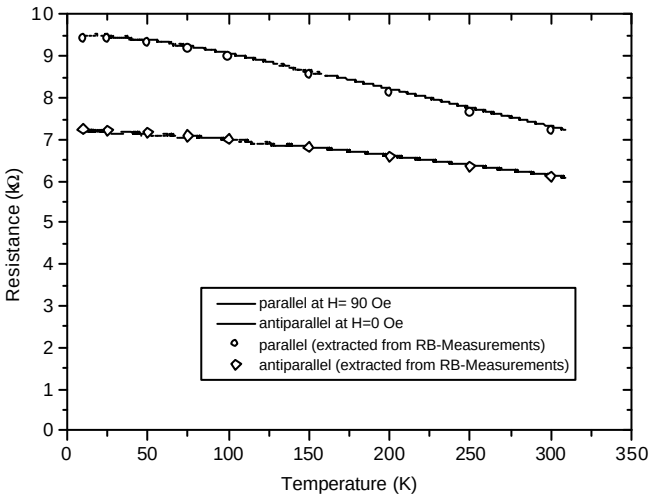

Figure 6.6 RT-measurements and resistances extracted from the RB-measurements.

With the extracted barrier width (*s*) and barrier height (*p*) from the JV-measurements (*s*=11 Å and *p*=2.6 Å) a normalised RT-curve is calculated with equation (2.45) of chapter 2, where the resistance at 5 K is set to unity.

The normalised RT-measurements of the parallel alignment and the antiparallel alignment are shown in figure 6.7 as two solid curves. The measurements deviate strongly from the calculated RT-curve. For completeness also the curve of the aluminium junction of chapter 5 is given in the figure, for which the same conclusion holds.

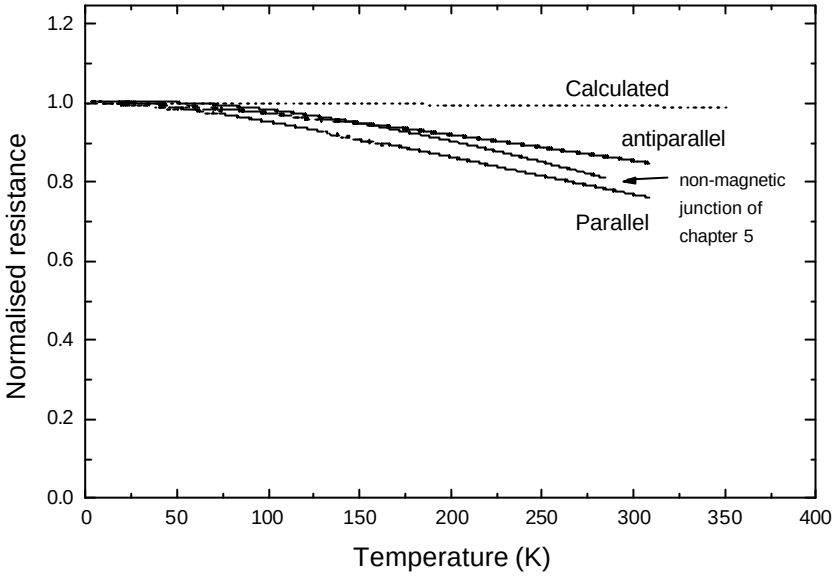

Figure 6.7 RT-measurement as compared to calculated measurement.

To account for this discrepancy we have extracted a spin-independent conductivity, G_{SI}, from the measurements, in the same way as described in chapter 4. This G_{SI} is described by a power law $G_{SI} = T^{g}$ and g becomes $g = 1.6$ which is slightly higher than found by Chang et al. [11], which was $g = 1.35 \pm 0.15$ for a magnetic $Co/Al_2O_3/Co$ junction.

In the theory of Chang et al. a hopping process via one atom ($N=1$) corresponds to $g = 4/3$ and at $N=2$ gamma corresponds to $g = 5/2$. There is a possibility that in our junction with $g = 1.6$ both hopping processes with $N=1$ and $N=2$ occur simultaneously to explain the data. Additional measurements are however required to look at the prediction more profoundly.

6.1.4 ΔG and JMR

Figure 6.8 shows the Junction MagnetoResistance (JMR) and the DG ($=G_a-G_p$) as a function of the temperature. Also the data obtained by the RB-measurements (the open circles) are included in the figure. The JMR decreases as the temperature increases: A JMR effect of 31% is observed at 10 K decreasing to 18 % at room temperature. This is probably caused by the decrease of the polarisation as a function of the temperature as we mentioned in chapter 3.

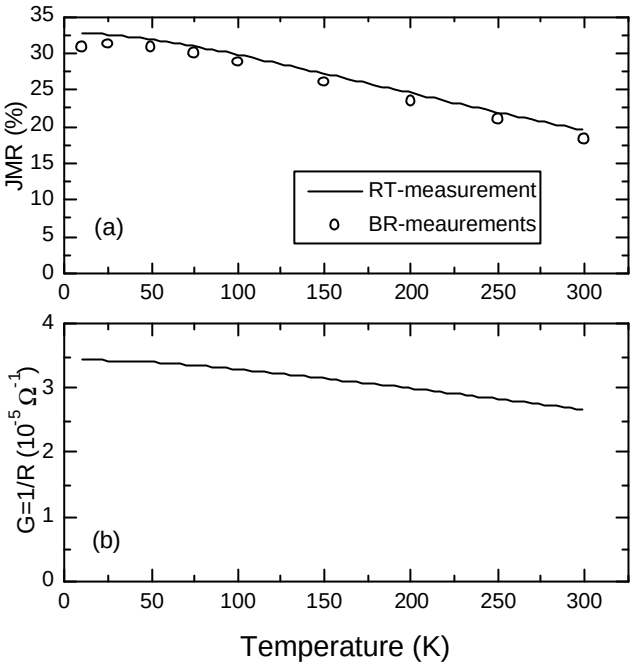

Figure 6.8 (a) JMR and (b) DG as a function of the temperature.

Equation (3.9) defines ΔG as a function of the temperature as $2G_T P_{Co} P_{NiFe}$ where $P_{Co}=P_{0\,K,Co}(1-\alpha_{Co}T^{3/2})$ and $P_{NiFe}=P_{0\,K,NiFe}(1-\alpha_{NiFe}T^{3/2})$. A numerical fit to the measured ΔG, shown in figure 3.10, gives $\alpha_{Co}=(10\pm5)\times10^{-6}$ $K^{-3/2}$ and $\alpha_{NiFe}=(3.6\pm0.4)\times10^{-5}$ $K^{-3/2}$ which compares reasonable with the values of Chang et al. for similar junctions [11]: $\alpha_{Co}=1\sim6\times10^{-6}$ $K^{-3/2}$ and $\alpha_{NiFe}=3\sim5\times10^{-5}$ $K^{-3/2}$. The dotted line in the figure gives the calculated *DG* as derived by this equation. The calculated *DG* is in reasonable agreement with the data, except for the lowest temperatures.

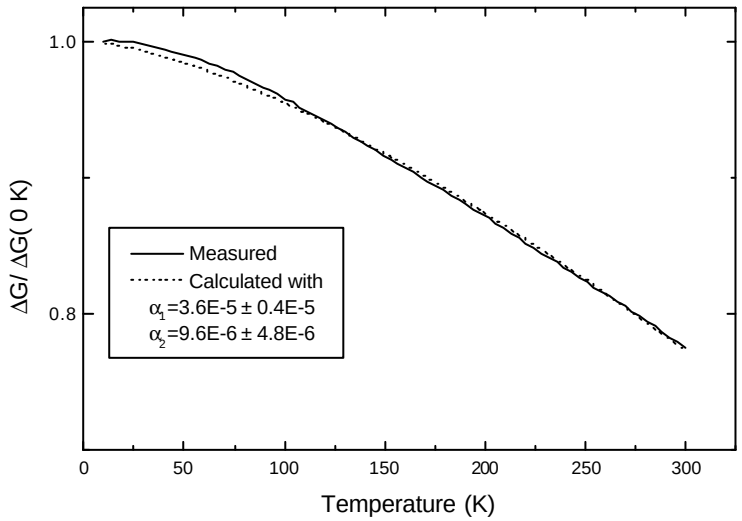

Figure 6.9 A numerical fit to the measured DG.

6.2 Coupling measurements

As we will see below, the Al and Al_2O_3 interlayers between the two magnetic layers may be thin enough to induce a ferromagnetic magnetic coupling. The magnetic coupling is the effect that the magnetic switching behaviour of the ferromagnetic top and bottom layer are changed, which will be investigated as a function of the temperature. If the coupling is very strong, both layers will act as one magnetic unit and the coercive fields of both layers are the same. If the coupling is weak, the shift of the coercive fields is a direct measure of the coupling strength.

6.2.1 Measurement of coupling by a minor hysterese loop

The strength of coupling between the two magnetic layers across the insulator can be measured by a minor hysteresis loop. In a minor hysteresis loop only the layer with the smallest coercive field switches and the other electrode with the highest coercive field keeps its magnetisation direction. An example of a measurement of a minor hysteresis loop is shown in figure 6.10a and 6.10c, where the electrode with the highest coercive fields (denoted by the black arrows) is negatively and positively polarised, respectively, during whole the entire hysteresis loop. The RB-loop in figure 6.10b, shows a complete hysteresis loop of the same sample.

The minor hysteresis shown in figure 6.10c, starts at the antiparallel alignment and in a negative field (a), whereby the resistance is high. This is also measured in the complete hysteresis loop in figure 3.4b at the antiparallel alignment. Then the field is increased and after it becomes positive the electrode with the smallest H_c switches (denoted as the grey arrow) at a field H_R, and the electrodes have a parallel magnetisation (b). The field is decreased (c) and after it becomes negative again, the electrode with the smallest H_c switches at a field H_L. The magnetic alignment of the electrode becomes antiparallel (d), which causes the resistance to rise. At the end of the minor loop, the magnetic field is the same as in the begin of the loop (a).

The magnetic coupling causes a shift of the coercive fields of the minor loops, defined as:

$$H_{shift} = \frac{H_L + H_R}{2} . \qquad (6.1)$$

If there is no coupling of the layer there is no shift (H_{shift}=0 Oe). If there is a ferromagnetic coupling between the electrodes, the H_{shift} is in the opposite direction of the magnetisation of the electrode with the highest coercive field. In other words an additional field is required when one wants to switch the magnetisation direction of one of the ferromagnetically coupled parallel aligned electrodes In figure 3.4c the H_{shift} is –1.9 Oe and, because the magnetisation of the layer H_c is positively directed, this junction shows a ferromagnetic coupling.

Figure 3.4a also shows a minor loop, but with the electrode with the highest coercive field directed in the other direction. In this example, this minor loop the H_{shift} is smaller and approximately 0.1 Oe.

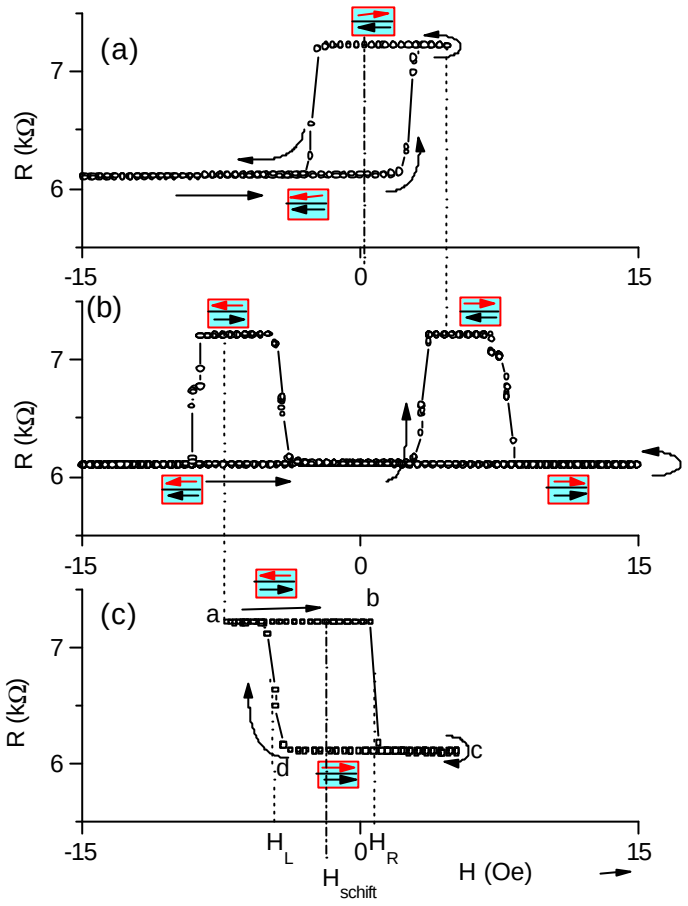

Figure 6.10 An example of a measurements with a minor hysteresis loop at 300 K.

If one assumes a single magnetic domain in each magnetic layer, with magnetisation only parallel or antiparallel to the applied field, the exchange coupling constant J (in J/m^2) is [9]:

$$J = H_{shift} m_0 t M \,, \tag{6.2}$$

where t is the thickness and M the saturation magnetisation of the electrode with low reversal fields.

6.2.2 Results

As we have explained before, in one minor hysteresis loop the soft-magnetic NiFe top electrode turns its magnetisation direction, while the hard-magnetic Co bottom electrode keeps its magnetisation direction. A series of minor RB-hysteresis loops is measured at different temperatures between 10 K to 300 K. A few of those measurements with a negative polarisation of the hard magnetic electrode are shown in figure 6.11.

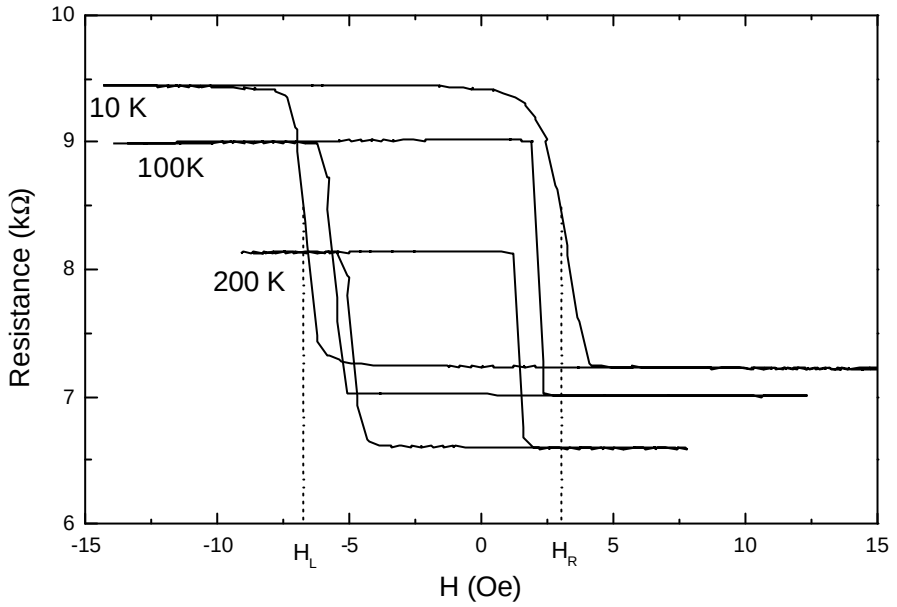

Figure 6.11 An example of measurements of minor RB-loops, where the Co bottom electrode is positively polarised. The NiFe top electrode changes its magnetisation direction.

From the minor loops the coercive fields are determined by the midpoints of the upper or lower flanks of the hysteresis loops. In figure 6.11 an example is shown for a minor loop at 10 K. The resulting coercive fields from one minor hysteresis loop are a negative (H_L) and a positive (H_R) field. These are shown in figure 6.12 for a negatively polarised electrode and positively polarised Co electrode.

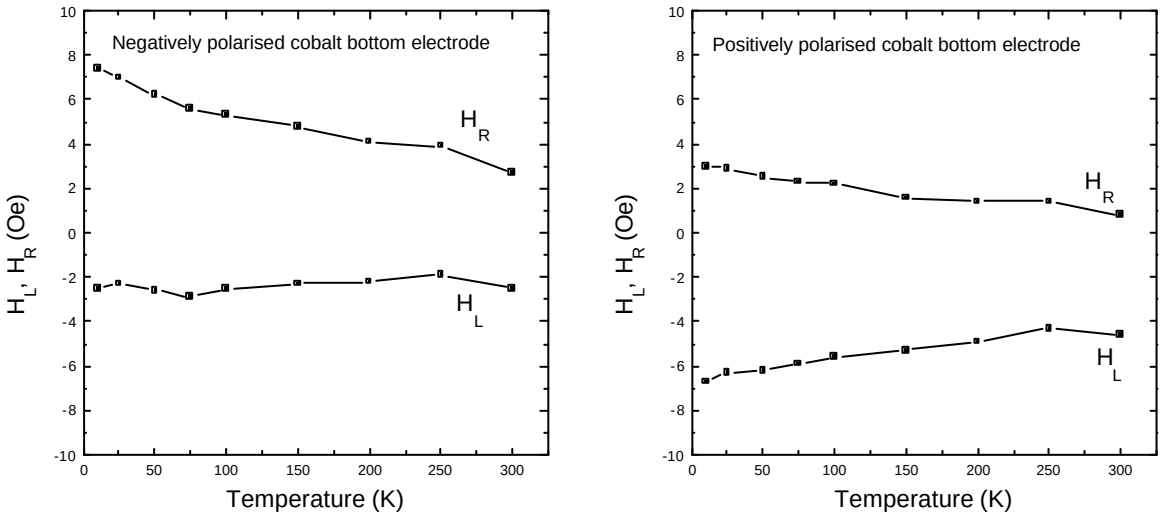

Figure 6.12 Measured coercive fields from minor hysteresis loops.

Finally, to derive the shift of the coercive fields, which is a measure for the coupling between the electrodes, one has to calculate the mean value of H_L and H_R of one minor hysteresis loop, as shown in figure 6.13.

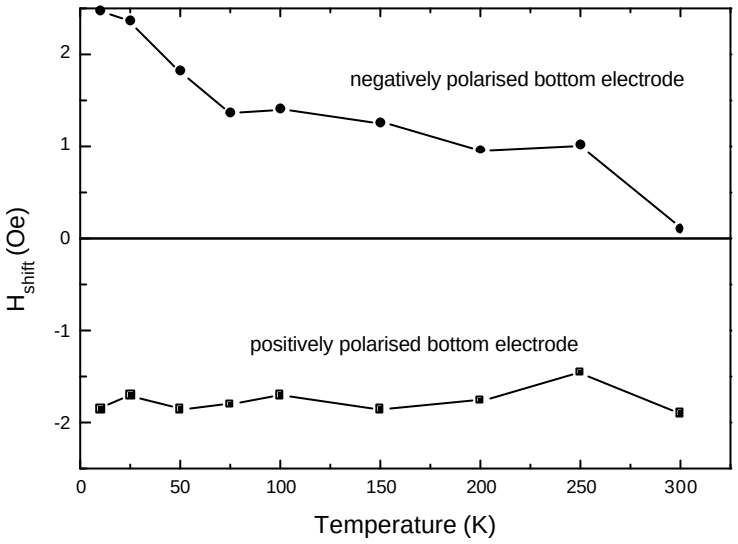

Figure 6.13 H_{shift} as a function of the temperature.

The shift of the minor loop with the negatively polarised bottom electrode becomes smaller (1-2 Oe) as the temperature rises. The shift with the positively polarised electrode remains approximately constant, although a small temperature dependence cannot be excluded. It is not yet understood why this difference in the upper and lower data sets are present. Note however, that the magnetic fields are extremely small, which may be the source for experimental errors.

In section 7.3.1 we will experimentally investigate the ferromagnetic coupling as a function of the oxidation time of the aluminium interlayer, where also the possible sources of the observed ferromagnetic coupling will be briefly described.

7 Results on magnetic tunnel junctions with variable oxidation time

7.1 Introduction

In reference [18] a series of junctions oxidised for 110 s with Al interlayer thicknesses in the range of zero to 25 Å has been investigated. Figure 7.1 shows the results of the measured JMR as a function of the interlayer thicknesses, where the optimal JMR was found with an Al interlayer thickness in the range of 10 to 16 Å. As concluded in the reference, for thin Al interlayers (<1.0 nm), it is possible that the Co bottom electrode becomes oxidised and CoO and/or Co_3O_4 is formed, which provides an additional semiconducting barrier. Moreover, Co-oxides are general magnetic which may enhance the mixing between the spin-up and spin-down electrons, the so called spin-flip scattering, This will reduce the overall JMR, as shown in figure 7.1.

On the other hand, aluminium interlayers with a thickness higher than 1.6 nm resulted in an unoxidised Al metal layer underneath an Al_2O_3 layer, which will also give a decrease of the observed JMR. According to reference [18], the polarisation of the ferromagnetic layer can be reduced by a metal layer at the interface with the barrier, thereby reducing the JMR.

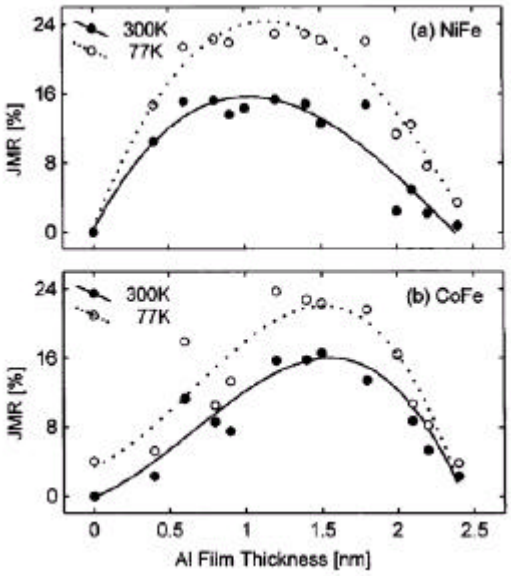

Figure 7.1 JMR plotted as a function of the thickness of the Al metal interlayer used to form the Al_2O_3 interlayer in Co/Al_2O_3/NiFe and Co/Al_2O_3/CoFe junctions. For all the junctions the Al-interlayer is oxidised for 110 s.

In this chapter the oxidation of an interlayer will be investigated further by the variation of the oxidation time when the Al-thickness is kept constant at approximately the optimum (10 to 16 Å). In detail, a series of tunnel junctions was prepared, where the oxidation time of a (12 Å) aluminium interlayer of the junction was varied in the range of 30 s to 490 s. The junctions have a Co bottom electrode with a thickness of 80 Å and a NiFe top electrode with a thickness of 80 Å. More details of the preparation process of this series is described in, section 4.2.

In the next section of this chapter the resistance and JMR of tunnel junctions as a function of the oxidation time of the Al interlayer will be described. Further it will be analysed whether a Co-oxide layer is formed at high oxidation times, as suggested in the reference [18].

The last section will characterise the magnetic coupling of the junctions that appears to be particularly important at short oxidation time, when the Al layer is not yet fully oxidised.

7.2 MagnetoResistance measurements

In this section we show the results of the measurements on the series of tunnel junctions, focussing on:

- Measurements of the resistance as a function of the temperature (RT-measurements).
- Measurements of the resistance as a function of the magnetic field (RB-measurements).
- Measurements of the current as a function of the applied voltage (JV-measurements).

7.2.1 Temperature dependence of the resistance

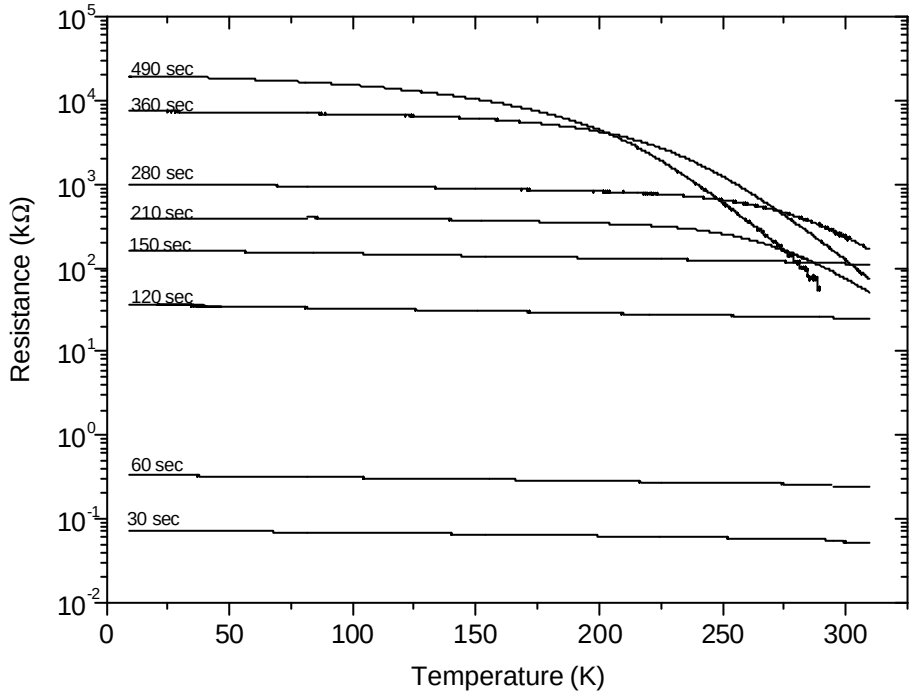

Figure 7.2 RT-measurements on junctions in the parallel alignment.

Figure 7.2 shows the RT-measurements on samples with oxidation times of the Al interlayer within the range of 30 s to 490 s. Since we anticipate on the possibility of Co-Oxide formation, which may be antiferromagnetic at low temperatures, in the ferromagnetic electrode a unidirectional magneto-anisotropy may be induced. The direction of this anisotropy depends strongly on how the system is

cooled through the antiferromagnetic transition temperature, and therefore we have always cooled down the junction in a field of 350 Oe parallel to the bottom electrode.

During the RT-measurements a field of 350 Oe is set, to direct the magnetisation directions of the bottom and the top electrode in the parallel direction. It is seen that the temperature dependence of the junction resistance with oxidation times t>150 s is much larger than for oxidation times t≤150 s: e.g the relative change in resistance between 10 K and 300 K is 22 % for an oxidation time of 60 s, while this is 82 % for an oxidation time of 280 s. The high temperature dependence at t>150 can be explained by the assumption that Co-oxide is formed, which is a semiconductor and therefore has a low barrier height. At low temperatures Co-oxide is acting as a barrier where only electrons can move through by tunnelling: the resistance of the junction is high. At ambient temperatures some electrons occupy energy states above the Co-oxide barrier, and therefore the Co-oxide becomes conductive: the resistance of the junction is low.

7.2.2 Resistance as a function of the magnetic field

Figure 7.3 shows an example of a measurement of the resistance as a function of the magnetic field (RB-measurement) of a junction with a 60 s, 150 s and 280 s oxidised Al interlayer, measured at 10 K and at 300 K.

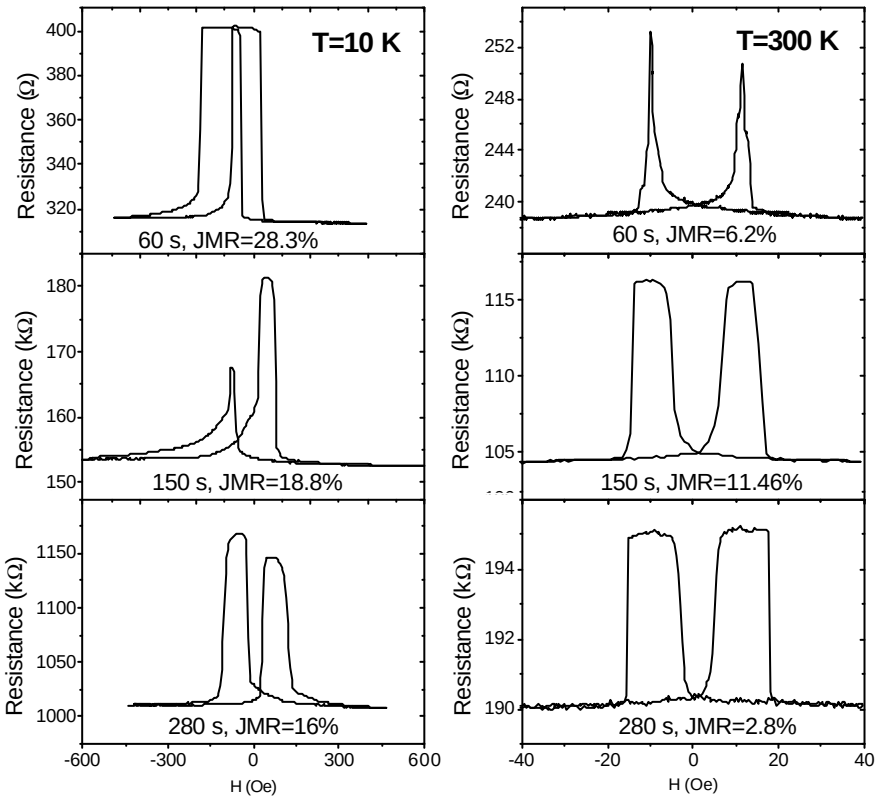

Figure 7.3 An example of RB-measurements of a 60 s, 150 s and 280 s oxidised sample at a temperature of 10 K and 300 K.

For each junction, both the JMR as well the resistance at 10 K are higher than at 300 K. The RB-curve is asymmetric at 10 K, while the curve at 300 K is symmetric. We think this asymmetry is probably

caused by a antiferromagnetic NiFe-oxide layer on top of the top-electrode, since it is oxidised by subsequent oxidation and deposition of the top-electrodes, as described in detail in section 4.1. Inherent to this preparation process, the samples with a short oxidation time therefore have a long oxidation of the NiFe top-electrode which gives NiFe-oxide. At low temperatures this oxide-layer becomes antiferromagnetic and this may cause a unidirectional anisotropy (exchange-biasing) of the NiFe layer seen as a shift of the hysteris loop.

It can also be seen in figure 7.3 that at 300 K and a short oxidation time of 60 s the magnetic layers do not switch separately but more like one magnetic unit. Section 7.3 will deal with this magnetic coupling.

For all oxidation times within the range of 30 s to 490 s, RB-measurements were performed. The JMR and resistances in the parallel state as a function of the oxidation time were extracted from the RB-measurements and are given in figure 7.4.

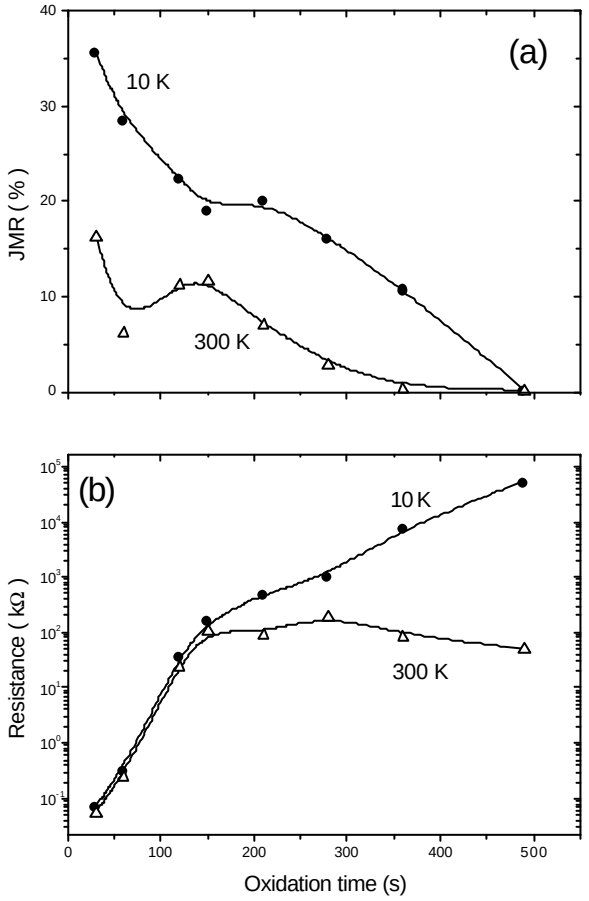

Figure 7.4 Results extracted from RB-measurements at Co(80 Å)/Al /NiFe (80 Å) junctions with different oxidation times of the 12 Å Al interlayer. (a) JMR as a function of oxidation time. (b) Resistance of the junction as a function of oxidation time, where the magnetisation of the electrodes are parallel aligned.

At 300 K we generally observe a lower JMR-ratio than at 10 K which we attributed to the temperature dependence of the polarisation direction due to the spin flip scattering. At around t=150 s we see the

smallest temperature dependence of JMR which is also comparable to the reduction observed in Chapter 6. For larger oxidation time t>150 s, the JMR drops much more significantly with temperature. This is to our opinion due to Co-oxide formation underneath the Al_2O_3. At high temperatures the paramagnetic Co-oxide is able to induce a large spin mixing at low temperature the magnetic ordering is re-established thereby reducing the spin flip scattering. So in general we observe that the reduction of JMR beyond 150 s is in accordance with the introduction of Co-oxide.

Probably at oxidation times t≤150 s a drop in JMR is masked by current distribution effects inducing a virtually high JMR-effect, because the resistance of the junction is in the same order as the resistance of the electrode (about 10 Ω) as described in reference [12]. Taken this enhanced JMR-effect into account, the optimal oxidation time of this junction is probably 150 s seen as the maximum at T=300 K. This is the oxidation time where all the aluminium is oxidised and no Co-oxide is formed.

This observations are confirmed by regarding the resistance at 10 K and at 300 K, see figure 7.4b. At the oxidation time t≤150 s the resistance is only slightly temperature-dependent, it only increases with the thickness due to oxidation of aluminium. At higher oxidation times, t>150 s, the largely different resistances of the junctions at 10 K and 300 K are due to the semiconductor character of Co-oxide which forms an extra tunnel barrier (and thus a higher resistance) when the temperature is low, and becomes conductive when the temperature gets high (with a not noticeable additional resistance).

At 10 K, both the resistances at t≤150 s and t>150 s rise exponentially as a function of the oxidation time. In section 2.2.4 we have seen that the resistance is exponentially dependent on the barrier width following the WKB-approximation, which would imply a constant growth rate during the Al-oxide formation as well during the formation of the underlying Co-oxide. However we can also see that the slopes of both log(R)-functions are different which indicates another growth rate (Co is less reactivity with O_2 than Al) and/or another barrier potential height of Co-oxide with respect to Al_2O_3.

7.2.3 Current as a function of applied voltage

Figure 7.5 shows a logarithmic presentation of JV-measurements of junctions with different oxidation times of the Al interlayer of the junction. The JV-measurements are made at 10 K and 300 K in the parallel orientation, due to the applied magnetic field of 350 Oe. Note that we also cooled down with a magnetic field of 350 Oe as mentioned in section 7.2.1.

The curves at 10 K have a decreasing current density (increasing resistance) as the oxidation time gets larger, in accordance with the previous section, which now appears to apply for all applied voltages. At 300 K the same happens for oxidation times t≤150 s, but for oxidation times t>150 s the curves at different T cross each other, which is due to the strong decrease of the resistance as shown also in the previous sections. But if we focus on the qualitative behaviour of the JV-curves we see that beyond t=150 s, where Co-oxide is formed, the curves becomes more rounded. To illustrate this better, we have plotted this in figure 7.6.

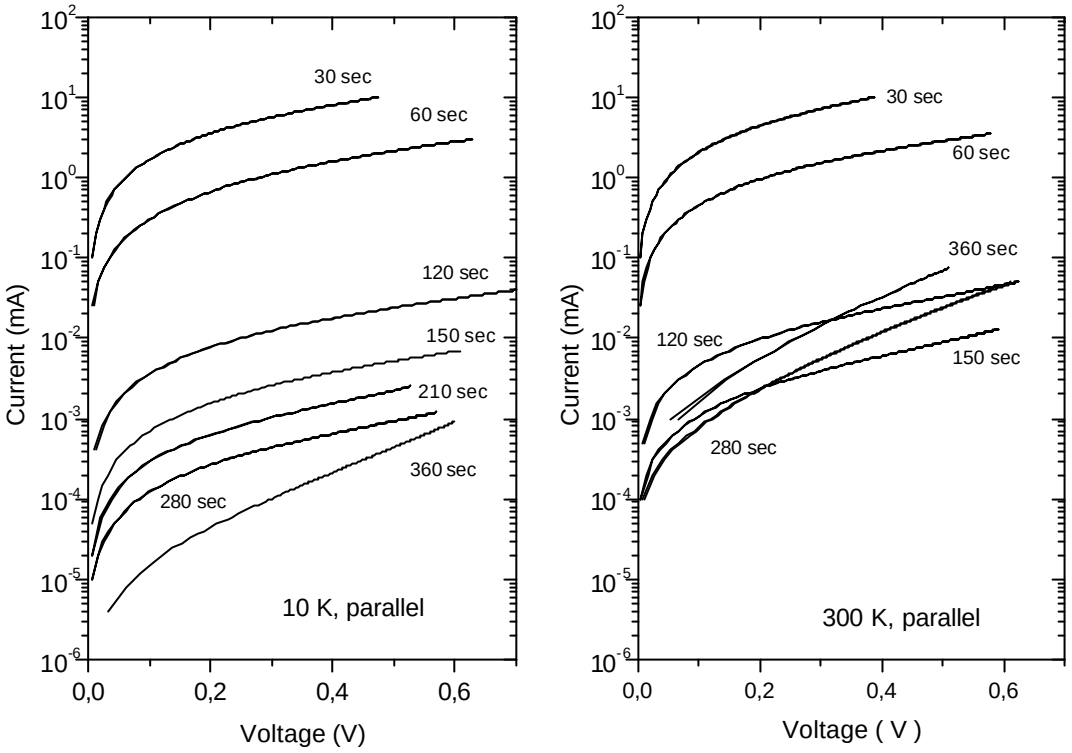

Figure 7.5 Presentation of IV-measurements of samples with various oxidation time in the range of 30 s and 360 s.

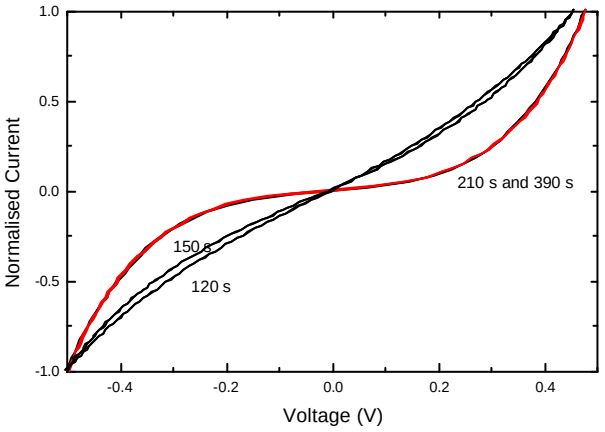

Figure 7.6 Normalised JV measurements at 300 K. The current density at –0.5 V is normalised to unity. The curves of 210 s and 390 s overlaps.

To quantify this, the barrier parameters of the junctions with oxidation times between 30 s and 490 s are extracted by using the Simmons and Brinkman equation for a numerical fit to the JV-curves in the parallel alignment. The extracted fit parameters, the barrier height (p) and barrier width (s) are shown in figure 7.7. The barrier parameters are extracted from JV-measurements in a range of 400 mV. Also

barrier parameters were deducted from other voltage ranges, which are shown in appendix F, and generally show a similar (qualitative) behaviour.

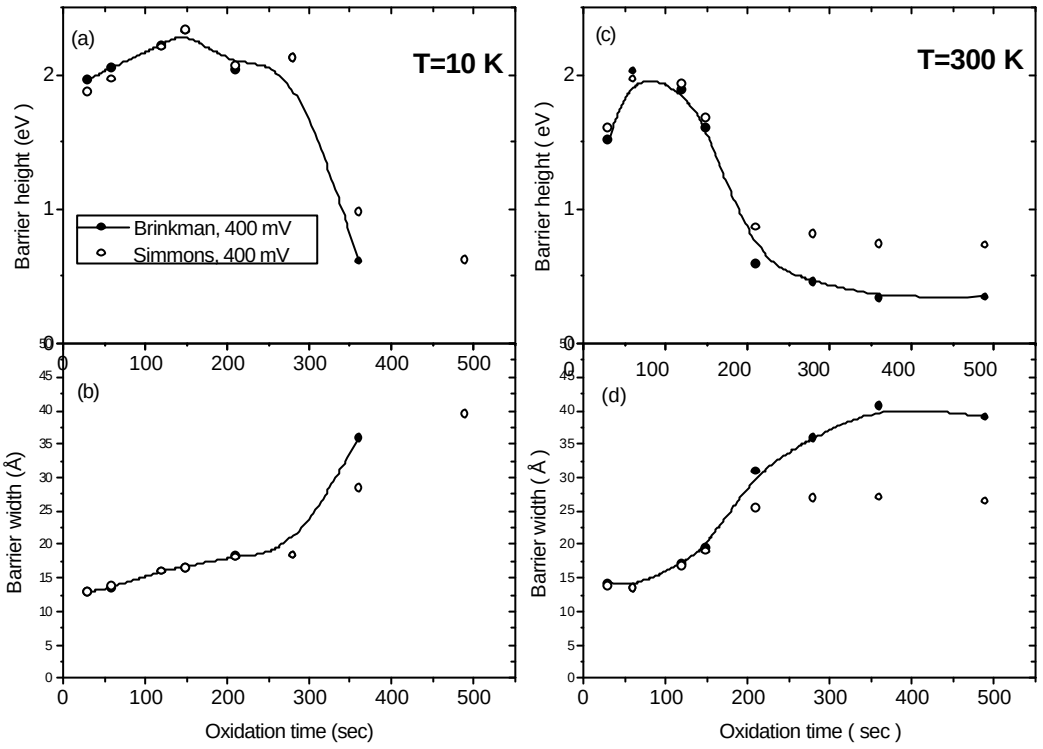

Figure 7.7 The potential barrier height and barrier width of the tunnel barrier as a function of the oxidation time. The parameters are extracted from the JV-measurements, by fitting with the Brinkman equation and Simmons equation.

To start with, it is difficult to conclude from the barrier parameters (section 7.2.2) that a Co-oxide layer is formed. It is questionable whether the fit equations can be still be used if an additional Co-oxide layer is present, which was not taken into account in theory. However by looking at figure 7.7 it can be seen that there is again a transition at around t=150 s, especially for T=300 K. In more detail we observe:

- The barrier width rises (both at 10 K and 300 K) from a minimum of 12 Å to a maximum of about 40 Å, as the oxidation time gets longer, which indicates that the barrier grows as a function of the oxidation time. Moreover for the Simmons parameters the growth rate of Co-oxide (at t>150 s) is higher then the growth rate of Al_2O_3 at t<=150 s. Because the insulator barrier with Co-oxide is lower than the barrier of Al_2O_3, the log(R) as a function of T has a smaller slope, as seen in section 7.2.2.
- If the oxidation time is t<=150 s, the barrier height stays approximately constant at about 2 eV, since in that oxidation region only Al_2O_3 is formed as a barrier. with a height of Al_2O_3 (as also found in chapter 6) approximately 2 eV. In chapter 6 at 10 K a barrier height of 3.0±0.5 eV was found for a junction with a 14 Å aluminium layer which was oxidised for 100 s. An probably explanation for the differences is the different range (600 mV) wherein the numerical fit was performed, where more details are shown in appendix F.
- If the oxidation time is t>150 s, the barrier height lowers since we add an additional barrier layer (Co-oxide) which probably affect the JV-curves. Theoretical calculations are in progress [6] to predict the impact of additional (non)magnetic layers at the junction on the JV-curves.

At an oxidation time of 150 s all the 12 Å aluminium is oxidised and no Co-oxide is formed, as concluded in the previous text. With this oxidation time, the barrier width is 16 Å, as can be seen in figure 7.7. It should be expected that the barrier width is somewhat thicker than 12 Å (the deposited Al-layer), because the oxidised aluminium layer is probably expanded. The extracted barrier width, extracted from a JV-measurement at 10 K, is 16 Å (as can be seen in figure 7.7) which corresponds reasonably well with the expected thickness.

Figure 7.8 shows the fit results of Brinkman of the asymmetric barrier height Δp. Some fitted asymmetrics are larger than the barrier height, which is, however, a very questionable result. Nevertheless, at high oxidation times the asymmetry is no longer present, which may also be due to the Co-oxide formation, although this is not yet clarified.

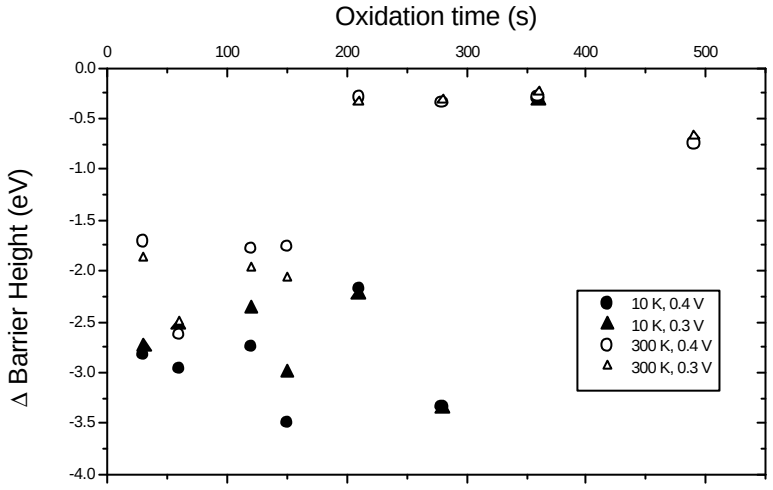

Figure 7.8 Barrier asymmetry height Dp as a result of the fit by the equation of Brinkman.

7.3 Magnetic analyses of the measurements

7.3.1 Coupling as a function of oxidation time

It was shown in figure 7.3 that at short oxidation time the magnetic layers do not switch separately but more like one magnetic unit. This may be due to an exchange coupling between the electrodes which will be investigated of a function of oxidation time in this section. The exchange coupling is not determined by a minor hysteresis loop of the resistance as function of the field, as described in chapter 6, but with the coercive fields of a complete hysteresis loop (RB-measurement), as shown in figure 7.9a. To verify the measured coercive field extracted from the RB-hysteresis loops, also measurements with MOKE were performed, as described in section 4.3 and in more detail in

reference [30]. An advantage of the MOKE measurements is that it is able to measure the coercive field on the electrode itself, and not only on the junction as the electrical RB-measurement does.

Figure 7.9 shows an RB-measurement compared with a MOKE-measurement on a junction which aluminium interlayer is oxidised for 150 s. The coercive field of both measurements are the same within a maximum error of 1 Oe.

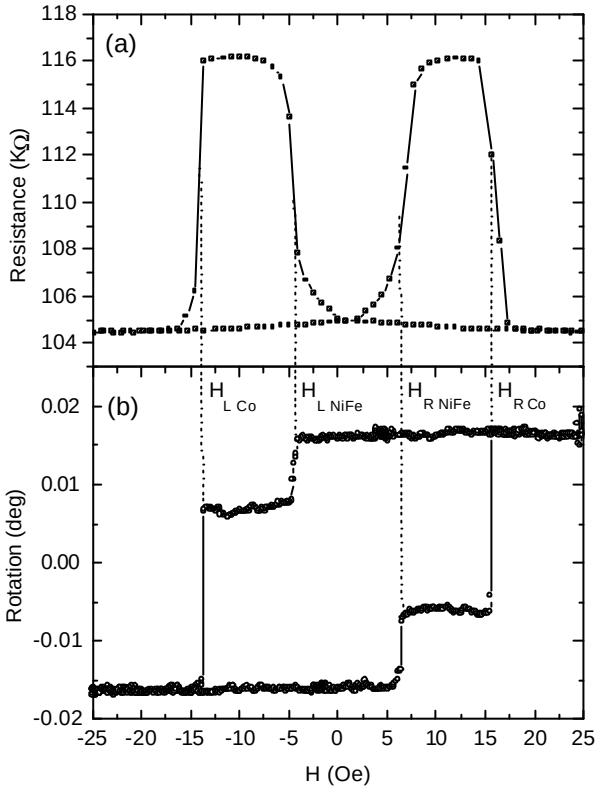

Figure 7.9 An RB-measurement (a) compared with a MOKE-measurement (b). Both measurement are performed at 300 K on a junction which is 150 s oxidised . The four different coercive fields ($H_{L\,Co}$, $H_{L\,NiFe}$, $H_{R\,NiFe}$, and $H_{R\,Co}$) are indicated in the figure.

From each measurement the coercive fields were determined by the field of the midpoint of the rising or falling edges of the junction hysteresis loops. In that way, four coercive fields are determined from an RB-measurement, as shown in figure 7.9, defined as $H_{L\,NiFe}$, $H_{L\,Co}$, $H_{R\,Co}$, and $H_{R\,NiFe}$ in which the type of electrode that switches is indicated in the subscript.

To minimise the experimental errors of the determined coercive fields of the Co bottom electrode and the NiFe top electrode the absolute coercive fields are averaged according to:

$$H_{Co} = \frac{|H_{L\,Co}| + |H_{R\,Co}|}{2} \text{ and } H_{NiFe} = \frac{|H_{L\,NiFe}| + |H_{R\,NiFe}|}{2}.$$

and shown in figure 7.10 by the open and closed symbols, respectively. Furthermore the coercive fields of the electrodes itself, are determined by MOKE, which measurements are also described in reference [31], and are shown as the crosses.

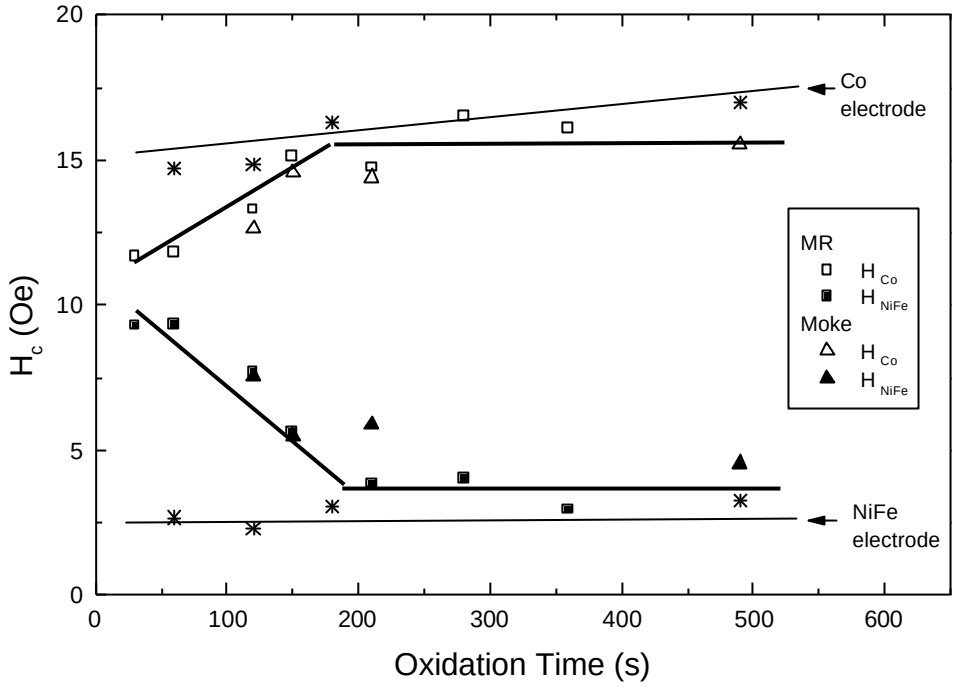

Figure 7.10 The mean absolute coercive fields of the Co bottom electrode and the NiFe top electrode at 300 K at the junction and at the electrodes. All the curves are guides to the eye only.

It can be concluded from figure 7.10 that at a small oxidation time (e.g 30 s) both layers are strongly coupled. At $t \leq 150$ s the decoupling is not yet fully accomplished. At t>150 s, where Co-oxide is formed in the interlayer, in approximation the electrodes switch at the same field as the junction itself.

The observed ferromagnetic coupling can have three reasons: (1) *magnetostatic coupling*, (2) *pinhole coupling* and (3) coupling due to the theory of *Slonczewski.* Those sources are described briefly below.

(1) A ferromagnetic magnetostatic coupling arises from correlated interface roughness which is schematically explained in figure 7.11, and is sometimes referred to as "*orange peel coupling*". It is possible that the roughness at the interfaces of the electrodes with aluminium decreases when it becomes Al_2O_3 during the oxidation process. As a consequence the coupling reduces as seen in the experiments.

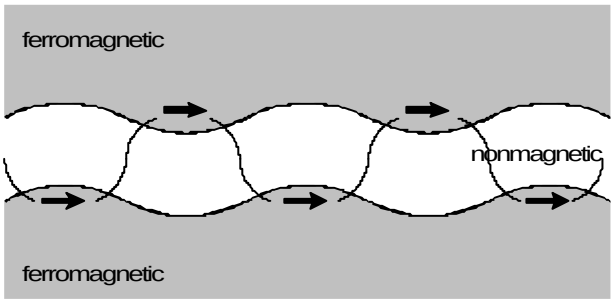

Figure 7.11 An example of a positively correlated ferromagnetic magnetostatic coupling of two ferromagnetic layers separated by a nonmagnetic layer.

(2) The direct contact of the magnetic layers caused by pinholes results in ferromagnetic coupling. Pinholes are metallic magnetic bridges between the magnetic layers across the space material. It

may be that pinholes are present in the tunnel junctions. Nevertheless, these pinholes have no noticeable effect on the electrical measurement, which indicate transport by tunnelling. At larger oxidation time the aluminium and the metallic bridges becomes oxidised, which would again explain the reduced coupling.

(3) The coupling of Slonczewski [8] is caused by the transmission of spin-polarised electrons from one conductor to the other through insulating spacers. This theory describes a coupling which is exponentially dependent on the insulator thickness. Since in our measurements the coupling depends of the insulator thickness (oxidation time) this Slonczewski coupling cannot be ruled out to account for the observed data.

More details about the coupling mechanisms are described in reference [19]. It is clear for this discussion that no indication is found in the measurements that favours one of the mentioned sources for coupling. Dedicated experiments, e.g. with the use of wedge-shaped spacers, should be performed to clarify the origin of the coupling between the electrodes in tunnel junctions.

7.3.2 Temperature dependence of JMR and coercivity of a junction with Co-oxide

To investigate the presence of Co-oxide formation at larger oxidation times the properties of one junction oxidised for 280 s, are investigated as a function of the temperature. Of this junction a series of resistance-magnetic field measurements were made at different temperatures [16], of which the JMR and the coercivity field of NiFe (H_c) is plotted in figure 5.12. H_c is calculated from the midpoint of the rising or falling edges of the junction hysteresis loop, which method also was used in the previous section. It can be seen that at temperatures below 150-200 K the Junction MagnetoResistance (JMR) remains constant, the coercive field rises significantly, and the resistance is not much T-dependent.

This can be understand qualitatively by an antiferromagnetic transition temperature in a thin Co-oxide layer. If $T<T_{af}$ the resistance is large and T-independent due to the Co-oxide barrier, the JMR stays roughly constant since the magnetic order in Co-oxide does not induce a large spin-flip scattering and the coercive field increases due to the onset of exchange coupling of the ferromagnetic Co, which is known to give rise to a increase of H_c [15]. When $T>T_{af}$ the resistance is strongly reduced due to the semiconducting character of Co-oxide, JMR becomes smaller by spinflip scattering at the paramagnetic Co-oxide an H_c reduces to small values usually seen in Co.

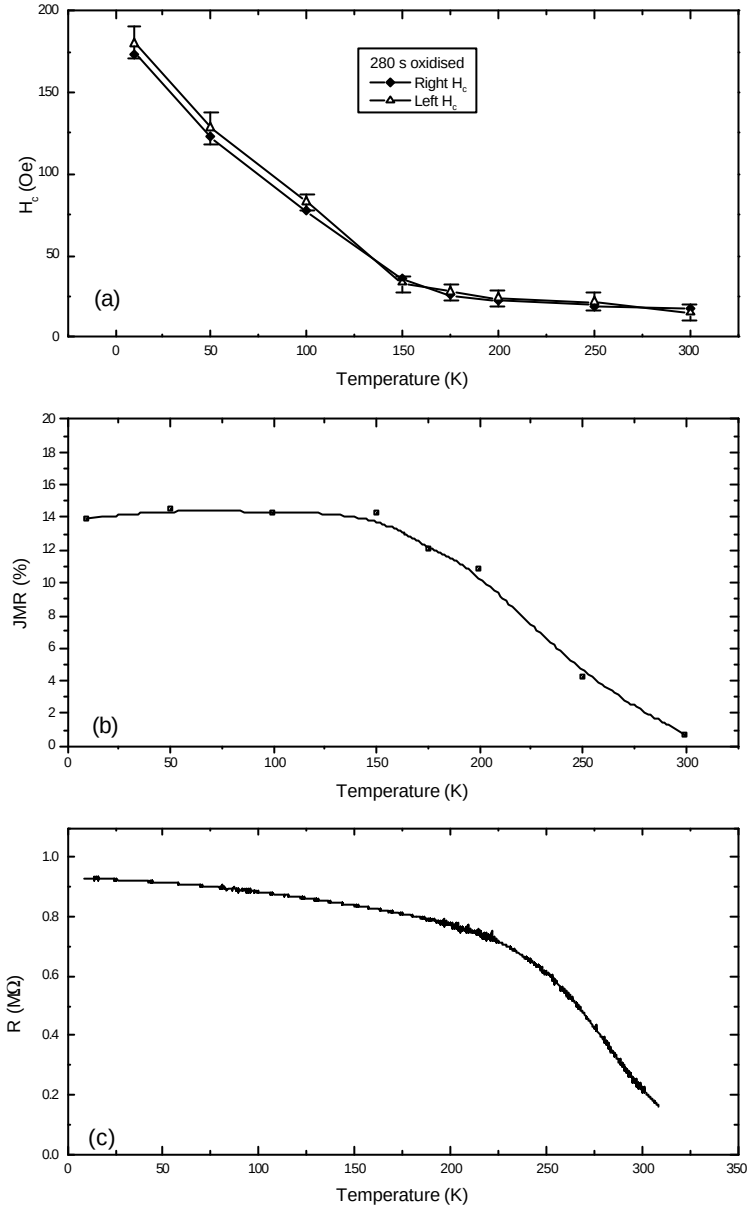

Figure 5.12 Temperature dependence of H_c (a), JMR (b) and R (c) for a 280 s oxidised junction.

8 Conclusion

Tunnel junctions grown at MIT have been electrically characterised at the University Eindhoven. The conclusions of this study are described below.

Theoretical

Both the *Simmons* and *Brinkman* model use the free electron approximation for the derivation of the current-voltage characteristics of tunnel junctions. We have found that the theoretical model of Simmons and that of Brinkman are equal for symmetric barriers at small voltages, because the second order Taylor expression of Simmons is the same as the equation of Brinkman. Due to a roughness of the surface of the insulator, the resistance as well as the current-voltage (JV)-curves of the junction are affected compared to a smooth surface as we derived in this report.

Experimental

In the electrical measurements the tunnel junctions are very sensitive for peak voltages and therefore several improvements had to be made before the MR-equipment was suitable to perform electrical measurements on tunnel junctions. A special device with needle spring probes was constructed, which contacts the electrodes of the tunnel junctions successfully. Although still only one junction at the time could be measured, this device has an advantage over silver paint contacts (contacting wires directly to the electrodes by conductive silverpaint). Contacting with spring probes is quicker and it is also possible to switch to an other junction on the set, without taking the sample holder out of the cryostat.

Extracting the barrier width and height with the equation of Simmons and Brinkman

It is indicated that the barrier width and height, extracted by a numerical fit of the formula of Simmons and Brinkman to the JV-masurements, are in reasonable agreement with the actual parameters of the barrier.

(1) First the established interlayer thickness during growth is in reasonable agreement with the extracted barrier width. Further in a Co(80 Å)/Al (12 Å, 150 s)/NiFe(150Å) junction, where all the aluminium is oxidised and no Co-oxide is formed, is investigated. The extracted barrier width of 16 Å corresponds reasonably with the expected value, which is somewhat thicker than 12 Å because the aluminium layer is probably expanded to a Al_2O_3 layer.
(2) In chapter 5 we concluded that the extracted *barrier height* of 2.0 eV of an Al(44 Å)/Al_2O_3(45 s)/Al(100 Å) junction corresponds with the barrier height found with photoemission by Nelson et al. [13]. For other junctions larger barrier heights have been found, of which the origin is not yet clarified.

In the description of JV-curves of magnetic tunnel junctions we should in principle take the splitting between the electron bands of spin-up and spin-down into account, which is not incorporated in the calculation of Simmons and Brinkman. Therefore the formulas of Brinkman and Simmons are less suitable to extract barrier parameters from JV-measurements, which can also be seen if one compares the measured dJ/dV-characteristics of a magnetic junction with the theoretical dJ/dV-characteristic of Simmons and Brinkman. Furthermore, the barrier height and width depend on the orientation of the electrodes, which is an unphysical situation. Nevertheless, the barrier width and height extracted from the equation is in reasonable agreement with the expectation.

The barrier parameters, found for an Al(44 Å)/Al_2O_3(45 s)/Al(100 Å) junction and a Co(80 Å)/Al (12 Å, 150 s)/NiFe(150Å) junction in chapter 5 and 6 respectively, extracted with the

formula's of Simmons and Brinkman, both have a small temperature dependence. The reason is that only exponential changes in the JV-characteristics give rise to a considerable difference in these parameters, which is not the case.

Temperature dependence of the resistance

For both, a nonmagnetic Al(44 Å)/Al_2O_3(45 s oxidised)/Al(100 Å) junction and a magnetic Co(80 Å)/Al_2O_3/NiFe(150 Å) junction, the temperature dependence of the resistance is much larger than that due to the broadening of the Fermi-Dirac distribution around the Fermi-level. An additional spin independent term (G_{SI}) has been added to the existing models, which describes measurements for both, magnetic and nonmagnetic, junctions reasonably well. The extracted power law dependence of G_{SI} with T^g of the spin independent term G_{SI} yields g =2.3 for a nonmagnetic and g =1.6 for a magnetic tunnel junction. This could mean a hopping mechanism for transport with N=2 for nonmagnetic and N=1 for magnetic tunnel junctions.

Temperature dependence of the JMR

In a Co(80 Å)/Al_2O_3/NiFe(150 Å) magnetic junction a JMR effect of 31% was observed at 10 K decreasing to 18% at room temperature. The model of Julliere for JMR had to be extended with a temperature dependent polarisation to account for this effect, where $P(T)=P(0\text{ K})(1-\alpha T^{3/2})$. A numerical fit to the data gives $\alpha_{Co}=(10\pm5)\times10^{-6}\text{ K}^{-3/2}$ and for $\alpha_{NiFe}=(3.6\pm0.4)\times10^{-5}\text{ K}^{-3/2}$, which compares reasonably with the values of Chang et al. [11] obtained on similar junctions: $\alpha_{Co}=1\sim6\times10^{-6}\text{ K}^{-3/2}$ and $\alpha_{NiFe}=3\sim5\times10^{-5}\text{ K}^{-3/2}$.

Oxidation time

In chapter 7 the electric and magnetic properties of a series of Co(80 Å)/Al /NiFe (80 Å) junctions are investigated, where the oxidation time of the 12 Å interlayer was varied between 30 s and 360 s. At $t\approx$150 s it seems that all the Al in the barrier is just oxidised, giving the best performances with respect to resistance and JMR. At higher oxidation times (t >150 s) the Co bottom electrode becomes oxidised and Co-oxides are formed. This provides an additional semiconducting barrier leading to a strong temperature dependend resistivity as compared to other junctions. Additionally, the formed Co-oxide decreases the JMR, attributed to the temperature dependence of the polarisation due to the spin flip scattering. At the oxidation time t<150 s not all the aluminium is oxidised and the JMR increases as the oxidation time gets shorter, which may be caused by the current distribution effect [12]. At 10 K, the resistance is exponentially dependent of the oxidation time, which indicates a constant barrier grow rate. Because the slopes of the log(R)-functions are different for $t\leq$150 s (where no Co-oxide is formed) and t>150 (where Co-oxide is formed) it can be concluded that Co-oxide has a different growth rate and/or an other barrier potential height.

Coupling

It is seen that the coupling of a Co(80 Å)/Al_2O_3/NiFe(150 Å) is ferromagnetic with a coupling field of NiFe of about 1-2 Oe and slightly decreases with temperature (chapter 6). Also the coupling as a function of the oxidation time (in chapter 7) was investigated, which is (at 300 K) strongest when much aluminium is still left in the barrier. As the oxidation time of the interlayer of the junctions rises, the coupling between two ferromagnetic layers decreases. Finally, at t>150 s, when the Al is no longer present and Co-oxide is formed, there is practically no coupling left. The observed ferromagnetic coupling can have three sources: magnetostatic coupling, pinhole coupling and coupling due to the theory of Slonczewski.

References

Theory of nonmagnetic junctions

[1] John G. Simmons, J. Appl. Phys. 34. 1793 (1963).

[2] John G. Simmons, J. Appl. Phys. 35. 2655 (1964).

[3] W. A. Harrison, Phys. Rev, **123**, 85 (1961).

[4] W. F. Brinkman, R. C. Dynes, and J. M. Rowell, J. Appl. Phys. **41**, 1915 (1970).

[5] Technical mathematics were performed by René van der Veerdonk and Bart Smits.

[6] Corné Kant, internal report, TUE, to appear in 1998.

Theory of magnetic tunnel junctions

[7] M. Julliere, “Tunneling between ferromagnetic films”, Phys. Lett., A **54**, number 3, 225-226, 1975.

[8] J. C. Slonczewski, Phys. Rev. B **39**, 6695 (1989).

[9] P. A. A. van der Heijden, P. J. H. Bloemen, J. M. Metselaar, R. M. Wolf, J. M. Gaines, J. T. W. M. van Eemeren, P. J. van der Zaag, W. J. M. de Jonge, Phys. Rev B **55**, 11 569 (1997).

[10] C. B. Duke, "Tunneling in Solids", Academic Press, New York, (1969).

[11] Chang He Shang, Janusz Nowak, Ronnie Jansen and Jagadeesh S. Moodera, “Temperature Dependance of Magnetoresistance and Surface Magnetization in Ferromagnetic Tunnel Junctions”, to be submitted.

[12] R. J. M. van de Veerdonk, J. Nowak, R. Meservey, J. S. Moodera and W. J. M. de Jonge, "Current distribution effect in magnetoresistive tunnel junctions.", Appl. Phys. Lett, **71,** 2839 (1997).

Measurements

[13] O. L. Nelson and D. E. Anderson, "Potential Barrier Parameters in Thin-Film Al-Al_2O_3-Metal Diodes", Journal of Applied Physics, **37**, 77 (1966).

[14] S. R. Pollack and C. E. Morris, "Electron Tunneling through Asymmetric Films of Thermally Grown Al_2O_3", Journal of Applied physics, **35**, 1503 (1964).

[15] R. Jungblut, R. Coehoorn, M. T. Johnson, J. aan de Stegge, and A. Reinders, “Orientational dependence of the exchange biasing in molecular-beam-epitaxy-grown Ni 80 Fe 20/ Fe 50 Mn 40 bilayers (invited)”, J. Appl.Pys, **75** (10), (1994).

[16] Measurements performed by Arjen Klaver with the MR-equipment at the TUE. For more information see his internal report at the TUE (to appear in 1998).

Optimum oxidation properties Al_2O_3 barrier

[17] J. S. Moodera and L. R. Kinder. "Ferromagnetic-insulator-ferromagnetic tunneling: Spin-dependent tunneling and large magnetoresistance in trilayer junctions (invited)", J. Appl. Phys, **79,** 4724 (1996).

[18] J. S. Moodera, E. F. Gallagher, Keziah Robinson, and J. Nowak, "Optimal tunnel barrier in ferromagnetic-insulator-ferromagnetic tunneling structures", Appl. Phys. Lett, **70,** 3050 (1997).

[19] J. M. Metselaar, "Interlayer coupling studies of two magnetite layers across different spacers", graduation report, TUE, (1996).

Assessment

[20] Gary A. Prinz, “Spin-Polarized Transport”, Physics Today, **58**, (1995).

[21] “The Non-Volatile Memory Challenge”, 84, Semiconductor International, (1997).

[22] W. J. Gallagher, S. S. P. Parkin, Yu Lu, X. P. Bian, A. Marley, K. P. Roche, R. A. Altman, S. A. Rishton, C. Jahnes, T. M. Shaw and T. M. Shaw and Gang Xiao, “Microstructured magnetic tunnel junctions”, Symposium on Magnetoelectric Devices for Information Storage, Gary Prinz, Chairman, J. Appl. Phys, (1997).

[23] patent No. 5650958: Magnetic tunnel junctions with controlled magnetic response. Inventors: Gallager, William Joseph, Parkin, Stuart Stephen Papworth, Slonczewski, John Casimir, Sun, Jonathan Zanhong, July 22, (1997).

[24] patent No. 5640343: Magnetic memory array using magnetic tunnel junction devices in the memory cells. Inventors: Gallagher, William Joseph, Kaufman, James Harvey, Parkin, Stuart Stephen Papworth, Scheuerlein, Roy Edwin, June 17, (1997).

[25] Mark Zellenrath, “Fabrication and Characterisation of ferromagnetic tunnel junctions”, Graduation report, Philips Research Laboratory, (1997).

MagnetoResistance-equipment

[26] P. P. L. Soetens, “Het automatiseren van een magneto weerstand opstelling", graduation report, Hogeschool Eindhoven, (1996).

[*27*] J. P. M. Hoefnagels, “Het operationeel maken van de IV-meting”, University Eindhoven, (1997).

Electrical breakdown

[28] W. Oepts, H. J. Verhagen, R. Coehoorn, and W. J. M. de Jonge, ”Dielectric Breakdown of Ferromagnetic Tunnel Junctions”, submitted to Appl.Phys. Lett. (1998).

[29] H. J. Verhagen, Graduation Report, TUE and Philips Research Laboratories, to appear in 1998.

MOKE

[30] M. M. H. Willekens "Giant Magnetoresistance in Spin Valves", Ph. D. thesis, TUE, (1997).

[31] C. Nuenen, Graduation report on MOKE and tunnel junctions , TUE, to appear in 1998.

[32] A. Rovers, Graduation report on MOKE and tunnel junctions, TUE, to appear in 1998.